Cell Reports

Article

An unsuspected physiological role for mGluRIII glutamate receptors in hippocampal area CA1

Graphical abstract

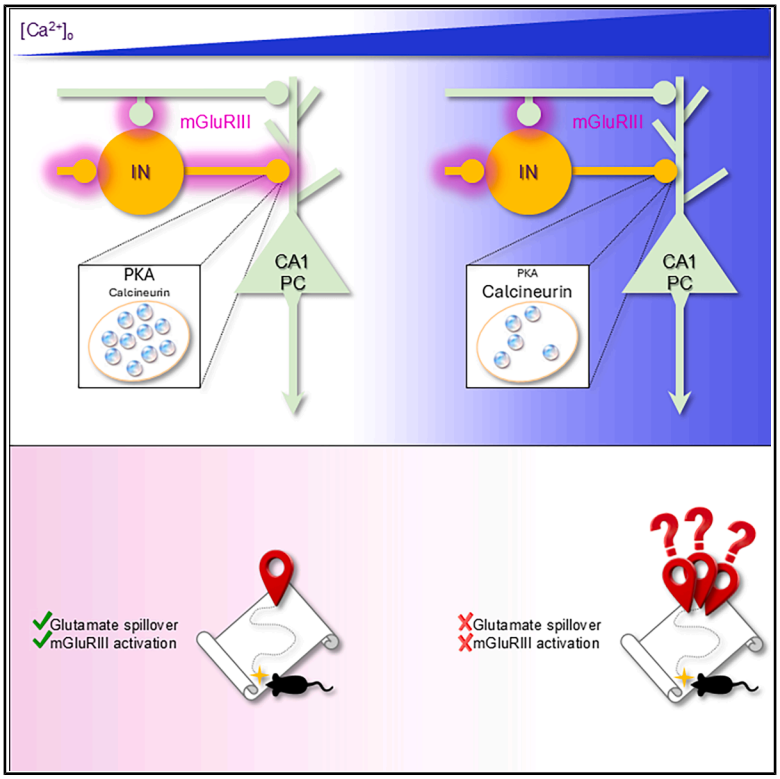

Highlights

- Lowering Ca^{2+} reveals spillover/mGluRIII-dependent suppression of inhibition onto CA1-PCs
- This effect is mediated by reduced, readily releasable size via PKA and synapsins
- *In vivo*, blocking mGluRIII or spillover reduces place field spatial specificity

Authors

Maurice A. Petroccione, Marcello Melone, Travis J. Rathwell, Namit Dwivedi, Christine Grienberger, Fiorenzo Conti, Annalisa Scimemi

Correspondence

scimemia@gmail.com

In brief

Petroccione et al. show that target-cell-specific modulation of excitation and inhibition onto CA1 pyramidal neurons, mediated by spillover activation of mGluRIII receptors, is lost at physiological extracellular calcium. *In vivo*, spillover and mGluRIII signaling improve the accuracy of the spatial representations of CA1 place cells.

Petroccione et al., 2026, Cell Reports *45*, 117388
June 23, 2026
https://doi.org/10.1016/j.celrep.2026.117388

CellPress

Cell Reports

CellPress
OPEN ACCESS

Article

An unsuspected physiological role for mGluRIII glutamate receptors in hippocampal area CA1

Maurice A. Petroccione,[1] Marcello Melone,[2,3] Travis J. Rathwell,[1] Namit Dwivedi,[1,4] Christine Grienberger,[5,6] Fiorenzo Conti,[2,3,6,8] and Annalisa Scimemi[1,6,7,9,*]

[1]SUNY Albany, Department of Biology, 1400 Washington Avenue, Albany, NY 12222, USA
[2]Università Politecnica delle Marche, Department of Experimental and Clinical Medicine, Via Tronto 10/a, 60126 Ancona, Italy
[3]IRCCS INRCA, Center for Neurobiology of Aging, Via Birarelli 8, 60121 Ancona, Italy
[4]IISER Pune, Dr. Homi Bhabha Road, Pune 411008, India
[5]Brandeis University, Department of Biology and Volen National Center for Complex Systems, Waltham, MA 02453, USA
[6]These authors contributed equally
[7]Senior author
[8]Present address: European Brain Research Institute (EBRI) Rita Levi-Montalcini, Viale Regina Elena 295, 00161 Rome, Italy
[9]Lead contact
*Correspondence: scimemia@gmail.com
https://doi.org/10.1016/j.celrep.2026.117388

SUMMARY

Group III metabotropic glutamate receptors (mGluRIII) are expressed broadly throughout the hippocampus but are thought to inhibit neurotransmitter release only at a subset of synapses and in a target-cell-specific manner. Here, we show that the supposed target-cell-specific modulation of GABA release only occurs when the extracellular calcium concentration in the recording solution is higher than its physiological value. Lowering extracellular calcium reveals an unsuspected mGluRIII-dependent suppression of inhibition onto CA1 pyramidal cells. This effect is due to a reduction in the size of the readily releasable pool, mediated by protein kinase A, and its vesicle-associated target proteins, synapsins. Using *in vivo* whole-cell recordings in behaving mice, we show that reducing spillover or blocking mGluRIII receptors in the intact CA1 network disrupts CA1 place cell activity. Together, these findings challenge our current understanding of the role of mGluRIII receptors in mediating hippocampal synaptic transmission and encoding spatial information.

INTRODUCTION

Group III metabotropic glutamate receptors (mGluRIII) are a family of G-protein-coupled receptors expressed widely throughout the brain. Ultrastructural studies in rats indicate that mGluRIII receptors are mainly localized in pre-synaptic terminals and axonal compartments.[1–13] Their primary role is to depress the release of glutamate, GABA, and neuromodulators, such as acetylcholine, monoamines, and peptides.[1–13] In the hippocampus, two types of mGluRIII receptors with high affinity for glutamate, mGluR4a (EC_{50} = 3–20 μM) and mGluR8a (EC_{50} = 0.02 μM), are expressed pre-synaptically, at both excitatory (E) and inhibitory (I) synaptic contacts.[9,10,12,14,15] By contrast, mGluR7a, a low-affinity mGluRIII type (EC_{50} = 1 mM), is thought to be expressed more abundantly at E compared to I pre-synaptic terminals and at pyramidal cell-to-interneuron (PC-IN) more than at pyramidal cell-to-pyramidal cell (PC-PC) synapses.[11] Consistent with this ultrastructural evidence, previous electrophysiology experiments in acute hippocampal slices showed that E/I synapses onto INs are more sensitive to mGluRIII modulation than E/I synapses formed onto PCs.[3,16] Because these effects could be detected in the presence of mGluRIII agonists like L-AP4 and in conditions that promote glutamate spillover (e.g., glutamate uptake blockers and repetitive stimulations), it was suggested that the mGluRIII-mediated inhibition of neurotransmitter release is activity-dependent and occurs only when the extracellular concentration of glutamate is increased from its baseline level.[3,16] Since mGluRIII receptors are coupled predominantly to $G_{i/o}$ proteins, their pre-synaptic l effect was thought to be mediated by inhibition of adenylyl cyclase, but more detailed information on the molecular mechanisms underlying this modulatory effect remained unclear.

When reviewing past slice physiology literature, an important methodological consideration is that many experiments have been performed using so-called "standard" extracellular recording solutions,[17] where the extracellular calcium concentration ($\left[Ca^{2+}\right]_o$) was set to 2–2.5 mM. This concentration range, which is more than 2-fold higher than what we now know to be present in the cerebrospinal fluid under physiological conditions (~1.2 mM),[18] was often chosen to facilitate neurotransmitter release, allowing the recording of larger currents.[19] Whether this masked an mGluRIII-dependent modulation of

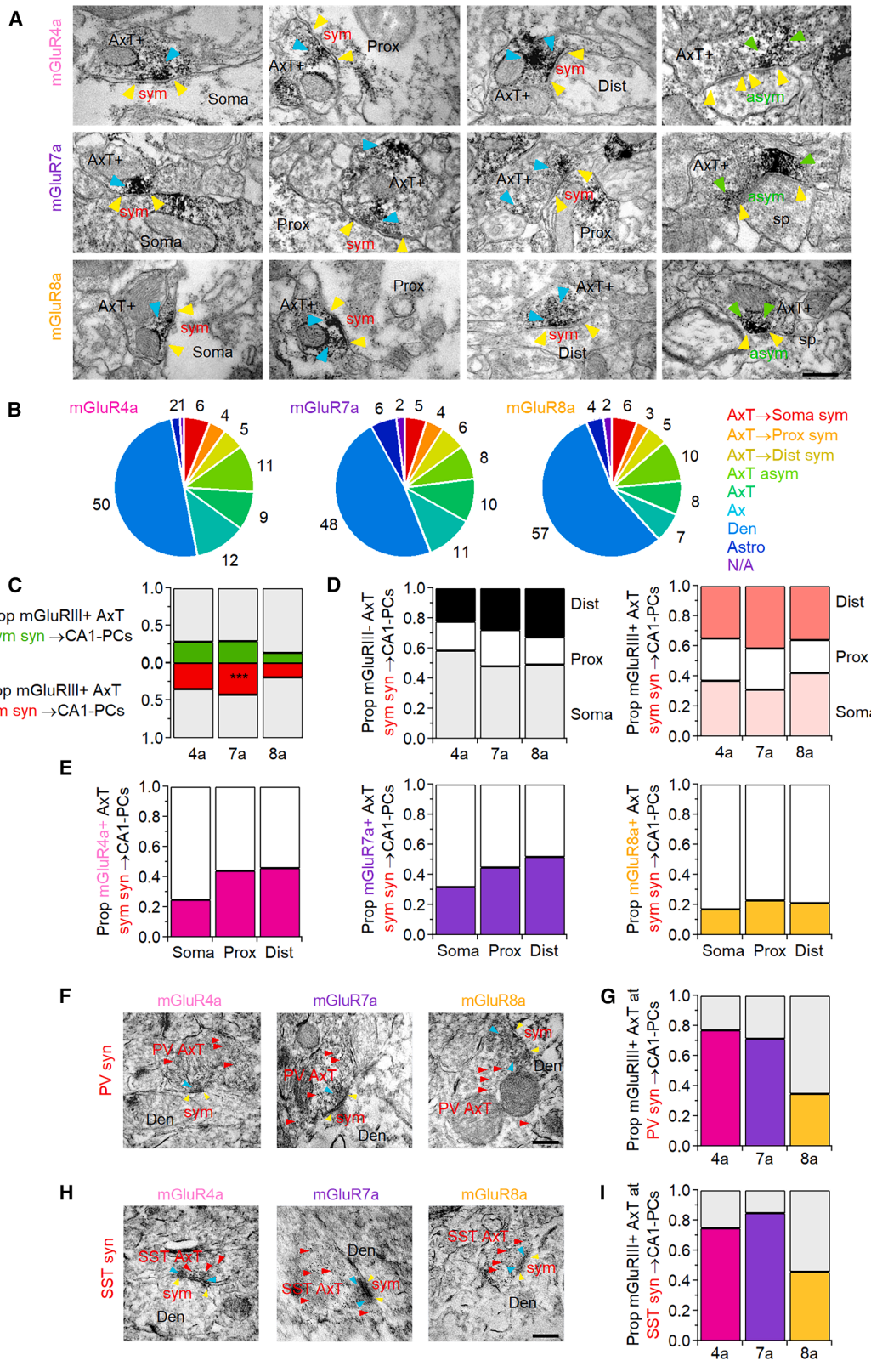

(legend on next page)

Table 1. Comparison of mGluR4a, mGluR7a, and mGluR8a localization at symmetric and asymmetric synapses onto CA1-PCs

Target	AxT profiles	AxT+ *sym*	AxT− sym	AxT+ *asym*	AxT− asym	*sym* vs. *asym*
mGluR4a	n = 743	35% n = 141	65% n = 263	29% n = 97	71% n = 242	p = 0.07
mGluR7a	n = 699	42% n = 154	58% n = 212	29% n = 89	71% n = 214	***p = 7.0e−4
mGluR8a	n = 662	19% n = 64	81% n = 267	14% n = 47	86% n = 284	p = 0.09

*p < 0.05, **p < 0.01, and ***p < 0.001 by Fisher exact test.

neurotransmitter release at E/I synapses onto CA1-PCs, to the best of our knowledge, has not been previously explored.

Here, we show that mGluRIII receptors are expressed at a subset of E/I synapses onto CA1-PCs and that under experimental conditions that mimic more closely the extracellular calcium concentration of the cerebrospinal fluid, the target-cell-specificity of the mGluRIII modulation of GABA release onto CA1-PCs is no longer detected. mGluRIII activation reduces synaptic inhibition from parvalbumin- and somatostatin-positive INs (PV- and SST-INs, respectively). By contrast, the target-cell-specific modulation of excitation by mGluRIII activation persists in $\left[Ca^{2+}\right]_e$ = 1.2 mM, leading to a reduced excitation of CA1-INs but not CA1-PCs. Finally, we examined the network effects of mGluRIII activation *in vivo,* showing that it limits location-specific firing of CA1-PCs, with important implications for their ability to generate accurate representations of spatial information in the hippocampus.

RESULTS

mGluRIII receptors are expressed at E/I synapses onto CA1-PCs

To analyze the sub-cellular distribution of mGluRIII in the mouse hippocampus, we used a pre-embedding electron microscopy (EM) approach and identified the ultrastructural localization of mGluR4a, mGluR7a, and mGluR8a at E and I synapses onto CA1-PCs, in the PC layer and *stratum radiatum*. Immunoreactivity for these receptors was localized to axons, axon terminals forming both asymmetric (glutamatergic, E) and symmetric (GABAergic, I) synaptic contacts, dendrites, and astrocytic processes (Figures 1A and 1B; Table S1). All mGluRIII receptor types were expressed pre- and post-synaptically (Figures 1A and 1B). We compared the degree of expression of each mGluRIII type at asymmetric versus symmetric synapses, to determine whether their abundance varies between E/I synapses onto CA1-PCs (Figure 1C). We then measured the proportion of mGluRIII immuno-positive and immuno-negative axon terminals onto CA1-PCs (mGluRIII+ and mGluRIII−, respectively; Figure 1C; Table 1) and found that, out of these three mGluRIII isoforms, mGluR7a was the only one that reached statistical significance for a preferential pre-synaptic expression at I synapses (***p = 7.0e−4). This was not the case for mGluR4a and mGluR8a, which showed a statistically similar level of pre-synaptic expression at E and I synapses onto CA1-PCs (p = 0.07 and p = 0.09, respectively; Table 1; Figure 1C).

The spatial distribution of mGluR4a+ and mGluR7a+ I terminals differed from that of mGluR4a− and mGluR7a− I terminals (***p = 1.6e−4 and **p = 2.9e−3, respectively; Table 2; Figure 1D). Most mGluR4a− and mGluR7a− I terminals were perisomatic (Figure 1D, left), whereas mGluR4a+ and mGluR7a+ I terminals were distributed similarly across the perisomatic compartment and proximal and distal dendrites (Figure 1D, right). mGluR8a+ and mGluR8a− I terminals were more likely to occur in the soma and distal dendrites compared to proximal dendrites (p = 0.55; Table 2; Figure 1D). Overall, the proportion of mGluR4a+ axon terminals increased from 25% at the soma to

Figure 1. Sub-cellular distribution of mGluRIII receptors at E/I synapses onto CA1-PCs

(A) Electron micrographs showing immuno-reactivity for mGluR4a, mGluR7a, and mGluR8a (cyan arrowheads) in the axon terminal (*AxT*) of asymmetric (*asym*) and symmetric (*sym*) synapses (margins labeled with yellow arrowheads) targeting the soma, proximal (*Prox*) and distal dendrites (*Dist*), and dendritic spines (*sp*) of CA1-PCs. Scale bars: 250 nm.

(B) Pie charts showing the quantification of the immunolabeling EM data. All mGluRIII receptors were expressed post- and pre-synaptically, especially at I synapses onto CA1-PCs. The number of technical replicates was n = 905, 1,056, and 472 for mGluR4a, mGluR7a, and mGluR8a, respectively. The number of biological replicates was N = 2.

(C) Summary of the proportion of E/I synapses (*syn*) onto CA1-PCs that are immuno-positive for different mGluRIII types. mGluR7a is more abundant at I than E synapses onto CA1-PCs. The number of technical replicates was n = 743, 699, and 662 for mGluR4a, mGluR7a, and mGluR8a, respectively. The number of biological replicates was N = 2.

(D) Left: summary of the spatial distribution of I synapses immuno-negative for different mGluRIII types. The number of technical replicates was n = 263, 212, and 267 for mGluR4a, mGluR7a, and mGluR8a, respectively. Right: summary of the spatial distribution of I synapses immuno-positive for different mGluRIII types. The number of technical replicates was n = 141, 154, and 64 for mGluR4a, mGluR7a, and mGluR8a, respectively.

(E) Proportion of analyzed I synapses that are immunopositive and -negative for mGluR4a (left), mGluR7a (center), and mGluR8a (right). For the left panel, the number of technical replicates was n = 206, 91, and 107 for soma, proximal, and distal dendrites, respectively. For the middle panel, the number of technical replicates was n = 150, 93, and 123 for soma, proximal, and distal dendrites, respectively. For the right panel, the number of technical replicates was n = 159, 62, and 110 for soma, proximal, and distal dendrites, respectively.

(F) Electron micrographs showing immunoreactivity for mGluR4a, mGluR7a, and mGluR8a (cyan arrowheads) in the axon terminal (AxT) of symmetric synapses formed by PV-INs (red arrowheads) onto the dendrites (Den) of CA1-PCs. Scale bars: 250 nm.

(G) Proportion of immunopositive PV synapses out of all those that were analyzed. The number of technical replicates was n = 26, 28, and 23 for mGluR4a, mGluR7a, and mGluR8a, respectively. The number of biological replicates was N = 2.

(H and I) As in (F) and (G) for synapses formed by SST-INs onto CA1-PCs. The number of technical replicates was n = 24, 33, and 24 for mGluR4a, mGluR7a, and mGluR8a, respectively. The number of biological replicates was N = 2. Scale bars: 250 nm. *p < 0.05, **p < 0.01, and ***p < 0.001 by Fisher exact test.

Table 2. Comparison of mGluR4a, mGluR7a, and mGluR8a localization at immunopositive (+) and immunonegative (−) axon terminals at symmetric synapses targeting the soma, proximal, and distal dendrites of CA1-PCs

Target	AxT profiles	*sym* ±	AxT>Soma	AxT>Prox	AxT>Dist	Difference across compartments
mGluR4a	*n* = 404	*sym*+ *n* = 141	37% *n* = 52 (25%)	28% *n* = 40 (44%)	35% *n* = 49 (46%)	***p = 1.6e−4
		sym− *n* = 263	59% *n* = 154 (75%)	19% *n* = 51 (56%)	22% *n* = 58 (54%)	
mGluR7a	*n* = 366	*sym*+ *n* = 154	31% *n* = 48 (32%)	27% *n* = 42 (45%)	42% *n* = 64 (52%)	**p = 2.9e−3
		sym− *n* = 212	48% *n* = 102 (68%)	24% *n* = 51 (55%)	28% *n* = 59 (48%)	
mGluR8a	*n* = 331	*sym*+ *n* = 64	42% *n* = 27 (17%)	22% *n* = 14 (23%)	36% *n* = 23 (21%)	p = 0.55
		sym− *n* = 267	49% *n* = 132 (83%)	18% *n* = 48 (77%)	33% *n* = 87 (79%)	

The percentage values represent the proportion of all immunepositive/immunonegative symmetric synapses present at the soma, proximal, and distal dendrites. The percentage values in parentheses represent the proportion of all somatic, proximal, and distal symmetric synapses immunopositive/immunonegative for each mGluRIII isoform. *p < 0.05, **p < 0.01, and ***p < 0.001 by Fisher exact test.

46% in distal dendrites (Figure 1E, left) and that of mGluR7a+ terminals increased from 32% at the soma to 52% in distal dendrites (Figure 1E, center). By contrast, the distribution of mGluR8a+ terminals did not vary significantly, being 17% at the soma and 21% in distal dendrites (Figure 1E, right).

Two major types of GABAergic interneurons (INs) in the hippocampus, the PV- and SST-INs, preferentially innervate the soma/proximal dendrites and distal dendrites of CA1-PCs, respectively.[20] By using a double immuno-peroxidase and pre-embedding immunogold labeling approach in tissue sections from *Pvalb*$^{Cre/+}$:*Gt(ROSA)26Sor*$^{tm9/+}$ and *Sst*$^{Cre/+}$:*Gt(ROSA)26-Sor*$^{tm9/+}$ mice, we found that most I terminals from PV- and SST-INs onto CA1-PCs express mGluR4a/7a (PV-INs: 71%–77%; SST-INs: 75%–85%), whereas only a subset of them expresses mGluR8a (PV-INs: 35%; SST-INs: 46%; Figures 1F–1I).

Together, these findings indicate that: (1) all mGluRIII receptor types are expressed pre- and post-synaptically; (2) mGluRIII receptors are expressed at a subset of E/I pre-synaptic terminals onto CA1-PCs; (3) mGluRIII+ I terminals target the soma, proximal, and distal dendrites of CA1-PCs; (4) mGluR4a and mGluR7a are the most abundant mGluRIII isoforms expressed at I synapses onto CA1-PCs; and (5) most I synapses onto CA1-PCs formed by PV- and SST-INs are mGluR4a+ and mGluR7a+, with a smaller proportion expressing mGluR8a.

mGluRIII activation reduces inhibition onto CA1-PCs at physiological $\left[Ca^{2+}\right]_o$

Despite ultrastructural evidence of mGluRIII expression at subsets of E/I synapses onto CA1-PCs, these receptors are thought to inhibit glutamate and GABA release only at E/I synapses targeting CA1-INs, based on experimental evidence collected under conditions that increase the concentration of glutamate in the extracellular space.[3,16] This conclusion, however, was reached based on experiments performed using solutions containing $\left[Ca^{2+}\right]_o$ = 2.5 mM. We confirmed this finding in our experiments, in which (1) we used $\left[Ca^{2+}\right]_o$ = 2.5 mM; (2) we increased the extracellular glutamate concentration by blocking GLT-1, the most abundant glutamate transporter in the adult brain, with DHK (100 μM)[21]; and (3) we evoked inhibitory post-synaptic currents (IPSCs) in CA1-PCs by delivering electrical stimuli to *stratum radiatum*. As shown in Figures 2A–2C, DHK did not lead to significant changes in the IPSC amplitude and kinetics when the $\left[Ca^{2+}\right]_o$ = 2.5 mM, in agreement with previous work[16] (amp: 93% ± 14%, p = 0.66; t_{50}: 105% ± 10%, p = 0.62; rise: 96% ± 10%, p = 0.73, n = 10). Since this $\left[Ca^{2+}\right]_o$ is more than 2-fold higher than the physiological $\left[Ca^{2+}\right]_o$ in the cerebrospinal fluid (i.e., 1.2 mM),[18] we repeated the experiments in $\left[Ca^{2+}\right]_o$ = 1.2 mM (Figures 2D–2F). In this case, DHK reduced the IPSC amplitude in CA1-PCs to 69% ± 6% of its baseline value (n = 15, ***p = 8.8e−5) without inducing any significant change in the IPSC decay and rise time (t_{50}: 93% ± 4%, p = 0.13; rise: 100% ± 7%, p = 0.96). To confirm that mGluRIII receptors mediated this effect, we applied DHK in the continued presence of the mGluRIII antagonist MSOP (100 μM). Under these conditions, DHK did not change the IPSC amplitude, decay, or rise time (amp: 98% ± 9%, p = 0.82; t_{50}: 91% ± 5%, p = 0.15; rise: 103% ± 16%, p = 0.88, n = 7; Figures 2G–2I). These findings suggest that: (1) blocking glutamate transporters promotes mGluRIII activation, and (2) in contrast to what was previously thought, when $\left[Ca^{2+}\right]_o$ is within the physiological range, spillover-mediated mGluRIII activation reduces GABAergic inhibition onto CA1-PCs. To determine whether this effect could be attributed to a particular type of mGluRIII receptor with very low affinity for glutamate and abundantly expressed in the CA1 area, like mGluR7a, we applied DHK in the continued presence of the mGluR7a antagonist MMPIP (10 μM). Under these conditions, DHK did not change the IPSC amplitude, decay, or rise time (amp: 101% ± 7%, p = 0.85; t_{50}: 100% ± 7%, p = 0.94;

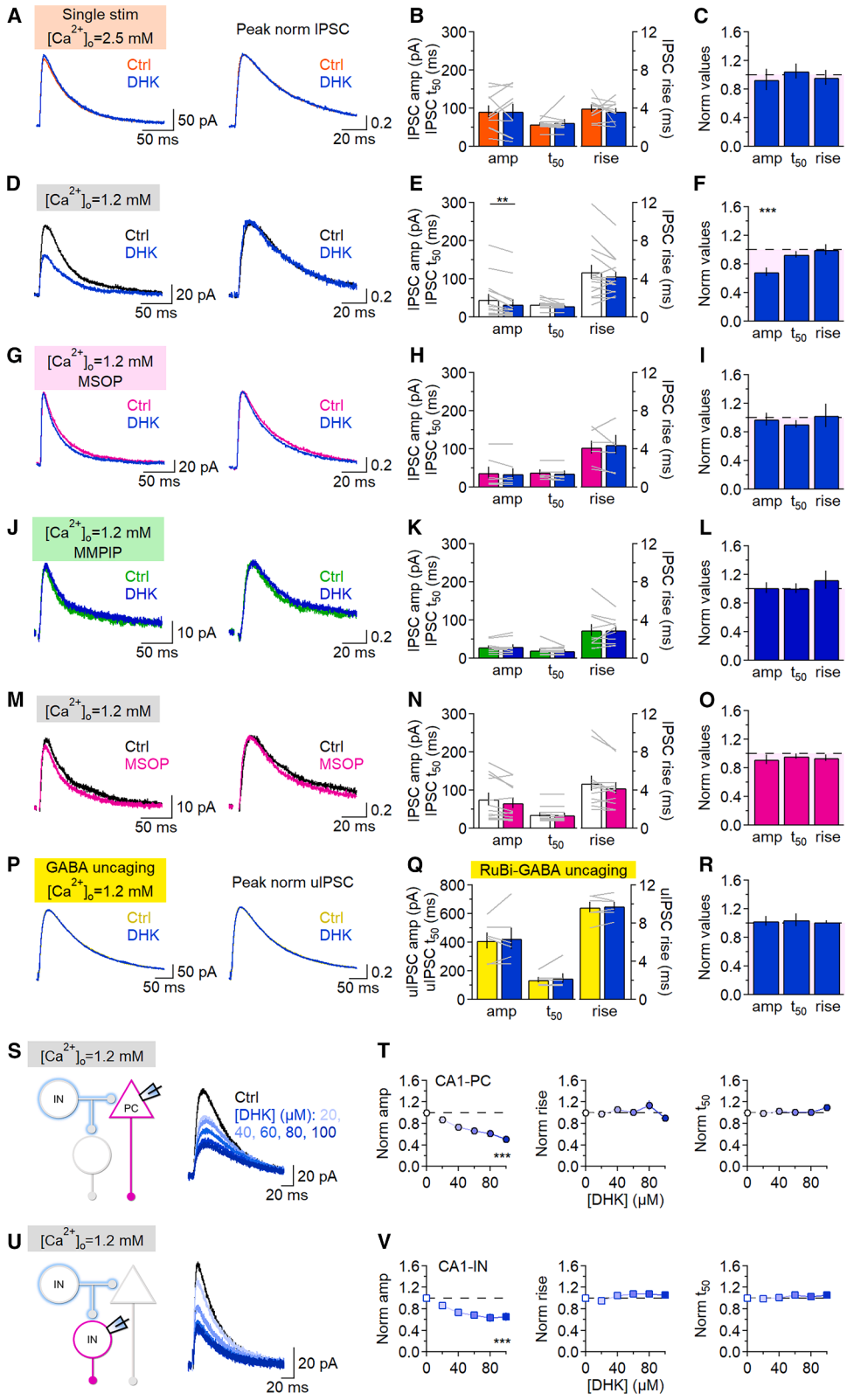

(legend on next page)

rise: 112% ± 13%, $p = 0.35$, $n = 10$; Figures 2J–2L), suggesting that the mGluRIII-dependent pre-synaptic inhibition of GABA release onto CA1-PCs is largely mediated by mGluR7a. Consistent with these findings, the IPSC amplitude was also decreased by CVN636 (1 μM), an allosteric agonist of mGluR7a receptors[22] (amp: 71% ± 4%, ***$p = 9.5e{-}5$; t_{50}: 95% ± 6%, $p = 0.44$; rise: 104% ± 8%, $p = 0.63$, $n = 9$; Figure S1). In slices, mGluRIII activation requires increased extracellular glutamate levels, because blocking mGluRIII receptors with MSOP in the absence of DHK did not change the amplitude and kinetics of IPSCs recorded from CA1-PCs (amp: 92% ± 6%, $p = 0.23$; t_{50}: 96% ± 3%, $p = 0.28$; rise: 94% ± 5%, $p = 0.25$, $n = 10$; Figures 2M–2O). We hypothesize that this might be due to fact that the slicing procedure, by severing cortical and intrahippocampal excitatory connections, might lead to reduced synaptic activity and a lower extracellular glutamate concentration than the one detected *in vivo*. Consistent with this, estimates of the extracellular glutamate concentration in slices suggest this is ~25 nM, whereas microdialysis experiments *in vivo* suggest this is in the low micromolar range (although this may also result from tissue damage around the microdialysis probe).[23] We addressed this concern later in this work through a series of experiments in awake-behaving mice.

To determine whether our findings held true throughout the neocortex, we repeated our experiments in principal cells of the primary somatosensory cortex (SS1-PCs). An mGluRIII-dependent suppression of heterosynaptic inhibition was still detected, suggesting that this modulation of inhibition is not limited to the CA1 region but also occurs in other cortical domains (Figure S2).

To rule out the possibility that the effect of DHK might be confounded by activation of post- rather than pre-synaptic mGluRIII, we performed a series of RuBi-GABA uncaging experiments ($n = 6$; Figures 2P–2R). In these experiments, blocking GLT-1 promotes the activation of both pre- and post-synaptic mGluRIII. However, since GABA is not released from pre-synaptic terminals, a reduction in the amplitude of uncaging evoked IPSCs (uIPSCs) induced by DHK would point to a post-synaptic contribution of mGluRIII, whereas the lack of effect of DHK on the uIPSC amplitude would suggest that activation of postsynaptic mGluRIII does not account for the results shown in Figures 2D–2F. To test this hypothesis, we blocked action potential propagation with TTX (1 μM) and evoked uIPSCs by uncaging RuBi-GABA (5 μM) onto CA1-PCs in the presence of ionotropic glutamate receptor blockers (NBQX 10 μM and APV 50 μM). uIPSCs were recorded in voltage-clamp mode, at a holding potential of 0 mV, the reversal potential of glutamatergic currents. Under these experimental conditions, DHK (100 μM) did not change the uIPSC amplitude and kinetics (amp: 103% ± 7%, $p = 0.64$; t_{50}: 105% ± 9%, $p = 0.63$; rise: 102% ± 2%, $p = 0.42$, $n = 6$; Figures 2P–2R). This suggests that the heterosynaptic depression of GABAergic inhibition onto CA1-PCs, induced by DHK and prevented by the simultaneous application of DHK and MSOP, is mediated by pre-synaptic mGluRIII.

We then asked whether GABAergic inhibition onto CA1-PCs and INs might have a different sensitivity to glutamate uptake blockade in $\left[Ca^{2+}\right]_o$ = 1.2 mM. To answer this question, we monitored the effect of increasing concentrations of DHK (20–100 μM) on IPSCs recorded from CA1-PCs ($n = 23$; Figures 2S and 2T) and *stratum radiatum* INs ($n = 19$; Figures 2U and 2V). All recordings were performed in the presence of NBQX (10 μM) and APV (50 μM), in cells voltage-clamped at 0 mV. The results showed that DHK reduced the IPSC amplitude similarly in CA1-PCs and INs ($p = 0.98$) without changing the IPSC kinetics (CA1-PC: rise $p = 0.97$, t_{50} $p = 0.99$; CA1-INs: rise $p = 0.23$, t_{50} $p = 0.49$). Together, these findings suggest that mGluRIII receptors do not inhibit GABA release in a target-cell-specific manner when the $\left[Ca^{2+}\right]_o$ = 1.2 mM, but reduce GABAergic inhibition similarly, onto both CA1-PCs and CA1-INs.

The expression of mGluRIII can also be detected at E synapses onto CA1-PCs, and even in this case, a target-cell-specific effect of mGluRIII activation has been detected in $\left[Ca^{2+}\right]_o$ = 2.5 mM.[3,24] For this reason, we asked whether DHK could induce a target-cell-specific change in the EPSC amplitude in $\left[Ca^{2+}\right]_o$ = 1.2 mM. EPSCs were pharmacologically isolated in the presence of the $GABA_A$ receptor antagonist picrotoxin (100 μM), at a holding potential of −70 mV. However, in

Figure 2. mGluRIII activation reduces inhibition onto CA1-PCs

(A) Average IPSCs recorded with $[Ca]_o^{2+}$ = 2.5 mM in CA1-PCs, before (orange) and after DHK (100 μM; blue). The traces on the right are normalized by the peak IPSC amplitude.

(B) Summary of the effect of DHK on the IPSC amplitude and kinetics. The number of technical replicates was $n = 10$. The number of biological replicates was $N = 5$.

(C) Summary of the relative change in IPSC amplitude and kinetics induced by DHK.

(D–L) As in (A–C), DHK was applied in the presence of $[Ca]_o^{2+}$ = 1.2 mM (D–F) and in the continued presence of MSOP (100 μM; G–I) or MMPIP (10 μM; J–L). In (E), the number of technical replicates was $n = 15$. The number of biological replicates was $N = 5$. In (H), the number of technical replicates was $n = 7$. The number of biological replicates was $N = 2$. In (K), the number of technical replicates was $n = 10$. The number of biological replicates was $N = 3$.

(M–O) As in (A–C), in baseline conditions and in the presence of MSOP. In (N), the number of technical replicates was $n = 10$. The number of biological replicates was $N = 7$.

(P–R) As in (A–C), for uIPSCs evoked by uncaging RuBi-GABA (5 μM) in $\left[Ca^{2+}\right]_o$ = 1.2 mM and in the presence of TTX (1 μM), NBQX (10 μM), and APV (50 μM), before and after DHK. In (Q), the number of technical replicates was $n = 6$. The number of biological replicates was $N = 2$.

(S) Schematic representation of the local circuit activated by the electrical stimulation when recording IPSCs from CA1-PCs. The traces represent average IPSCs recorded in the presence of increasing concentrations of DHK.

(T) Summary of the effect of different DHK concentrations on the amplitude, rise, and decay of IPSCs recorded from CA1-PCs. The number of technical replicates was $n = 23$. The number of biological replicates was $N = 11$.

(U and V) As in (S and T), for IPSCs recorded from CA1-INs in *stratum radiatum*. The number of technical replicates was $n = 19$. The number of biological replicates was $N = 8$. *$p < 0.05$, **$p < 0.01$, and ***$p < 0.001$ by paired *t* test for (A–R). *$p < 0.05$, **$p < 0.01$, ***$p < 0.001$ by GEE for (S–V). Data are represented as mean ± SEM.

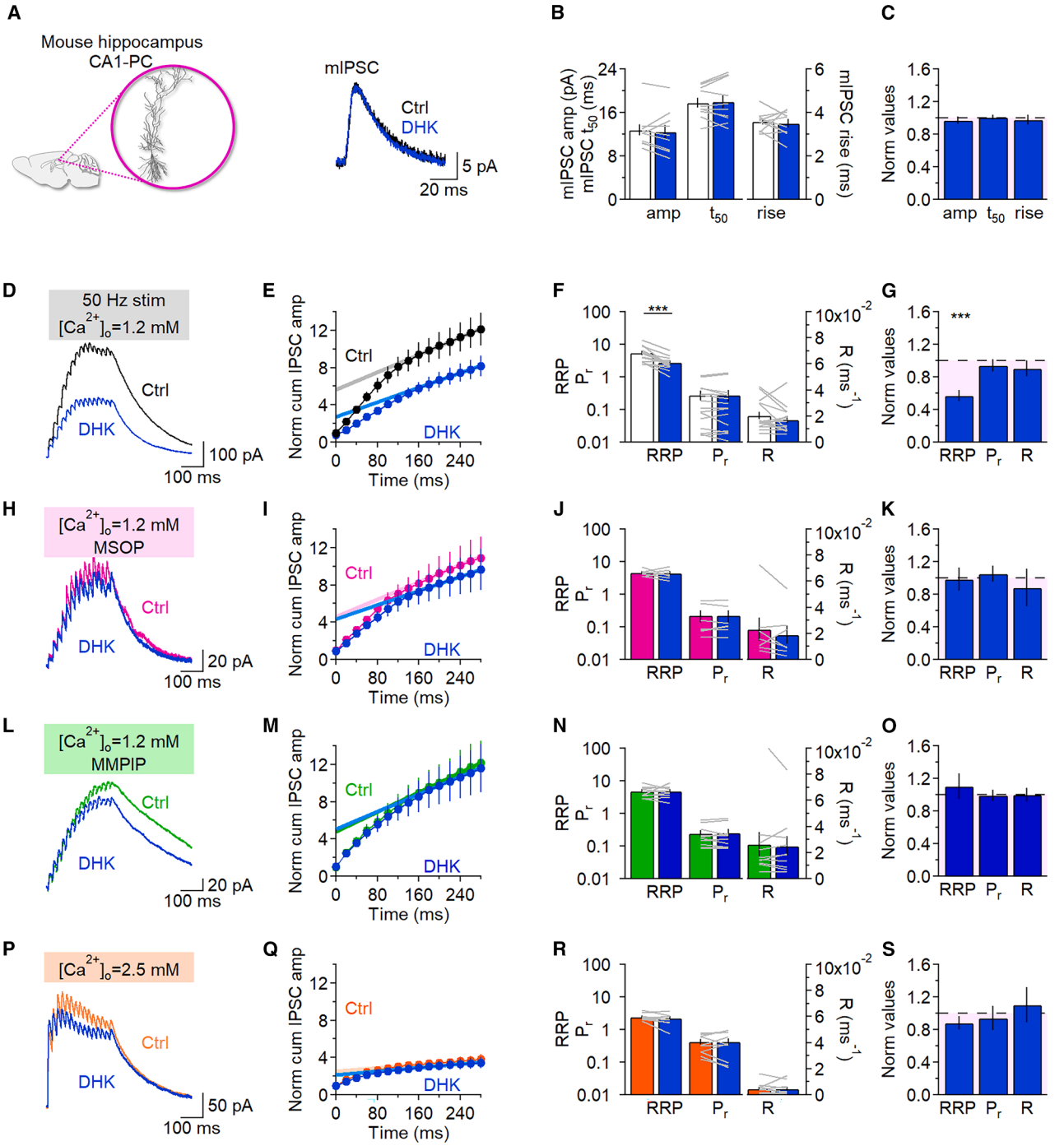

Figure 3. mGluRIII activation reduces the size of the RRP at I synapses onto CA1-PCs

(A) Left: schematic representation of CA1-PCs in sagittal brain slices. Right: average mIPSCs recorded in a CA1-PC in control conditions (black) and in DHK (100 μM; blue).

(B) Mean and in-cell comparison of the effect of DHK on the mIPSC amplitude and kinetics. The number of technical replicates was n = 10. The number of biological replicates was N = 2.

(C) Summary of the effect of DHK on the mIPSC amplitude and kinetics, normalized by their values in control conditions.

(D) Representative IPSC train recorded in response to *stratum radiatum* stimulation with 15 pulses at 50 Hz (280 ms), before (black) and after DHK (blue), in $[Ca^{2+}]_o$ = 1.2 mM.

(legend continued on next page)

$[Ca^{2+}]_o$ = 1.2 mM, DHK (100 μM) did not alter the EPSC amplitude, decay, and rise time in CA1-PCs (amp: 100% ± 16%, p = 0.98; t_{50}: 108% ± 4%, p = 0.07; rise: 107% ± 9%, p = 0.46, n = 10; Figures S3A–S3D), but induced a significant reduction of the EPSC amplitude in CA1-INs (amp: 42% ± 5%, ***p = 1.4e−5; t_{50}: 100% ± 16%, p = 1.00; rise: 98% ± 16%, p = 0.90, n = 8; Figures S3E–S3H). Similar results were obtained in $[Ca^{2+}]_o$ = 2.5 mM: DHK (100 μM) did not alter the EPSC amplitude, decay, and rise time in CA1-PCs (amp: 85% ± 17%, p = 0.41; t_{50}: 99% ± 5%, p = 0.81; rise: 103% ± 3%, p = 0.43, n = 14; Figures S3I–S3L), but induced a significant reduction of the EPSC amplitude in CA1-INs (amp: 57% ± 13%, ***p = 7.4e−3; t_{50}: 106% ± 15%, p = 0.69; rise: 100% ± 13%, p = 0.13, n = 10; Figures S3M–S3P). These findings suggest that rising levels of glutamate in the extracellular space can lead to a target-cell-specific reduction of excitation in CA1-IN, but not CA1-PCs, regardless of $[Ca^{2+}]_o$ (Figures S3Q and S3R).

mGluRIII activation reduces the size of the readily releasable pool

A reduction in the IPSC amplitude in the presence of DHK may be due to changes in the size of the readily releasable pool for GABA (*RRP*, comprised of *N* releases sites), the release probability (*Pr*), or the quantal size (*q*). To gain insights into whether promoting glutamate spillover with DHK led to changes in the quantal parameter *q*, we analyzed its effect on the amplitude of miniature IPSCs (mIPSCs), recorded from CA1-PCs in the presence of TTX (1 μM), NBQX (10 μM), and APV (50 μM), in cells clamped at 0 mV (Figures 3A–3C). The results showed that DHK (100 μM) does not change the mIPSC amplitude (97% ± 4%, n = 10, p = 0.48) or kinetics (t_{50}: 100% ± 3%, n = 10, p = 0.87; rise: 98% ± 6%, n = 10, p = 0.74; Figures 3B and 3C), suggesting that DHK does not change the quantal size, *q*.

We then delivered a train of 15 pulses at 50 Hz to *stratum radiatum* (Figures 3D–3S) and estimated the size of the *RRP* using a linear regression of the cumulative IPSC amplitude over time intervals that are short compared to the time required for recovery from synaptic depression.[25–29] The linear fit of the cumulative IPSC amplitude was performed on the last five IPSCs in the train. The replenishment rate *R* was estimated by the slope of the fit, whereas *Pr* was calculated from the ratio of the IPSC amplitude and the RRP size. The analysis indicated that, when $[Ca^{2+}]_o$ = 1.2 mM, DHK reduced the *RRP* size without altering *Pr* or the vesicle replenishment/refilling rate[30–34] ($RRP_{DHK/Ctrl}$: 57% ± 6%, n = 15, ***p = 1.0e−5; $Pr_{DHK/Ctrl}$: 94% ± 8%, p = 0.45; $R_{DHK/Ctrl}$: 91% ± 9%, p = 0.33; Figures 3D–3G). Similar results were also obtained when analyzing IPSCs recorded from SS1-PCs, indicating that similar mechanisms account for heterosynaptic depression of inhibition when glutamate uptake is impaired in different brain areas (Figure S4).

The regression analysis does not assume that *Pr* is constant throughout the train or uniform across all vesicles, but a potential caveat is that it assumes constant vesicle replenishment.[35] To account for potential inconsistencies in vesicle replenishment during the train stimulation, we verified the effect of DHK on the *RRP* using two other methods that rely on different assumptions.[29,36] For example, the EQ method[29] assumes that vesicle replenishment is negligible early during the train, when the synaptic currents decay linearly.[29] In this case, the *RRP* can be estimated by the *x*-axis intercept of a linear fit in a plot of the IPSC amplitude versus the cumulative IPSC amplitude during the train (Figures S5A and S5B). With the EQ method, the *RRP* in DHK was ∼79% of that in control conditions, with no significant change in the release probability *Pr* ($RRP_{DHK/Ctrl}$: 79% ± 5%, n = 15, ***p = 1.9e−5; $Pr_{DHK/Ctrl}$: 89% ± 6%, p = 0.08; Figures S5A and S5B).

A third method, referred to as the decay method, also allows estimating the *RRP* size, in this case from an exponential fit of the IPSC amplitude plotted against the stimulus number.[36] Using the decay method, we still found that DHK reduced the *RRP* size without altering *Pr* ($RRP_{DHK/Ctrl}$: 73% ± 11%, n = 15, *p = 0.04; $Pr_{DHK/Ctrl}$: 104% ± 23%, p = 0.14; Figures S5C and S5D). Together with the mIPSC analysis, these results indicate that experimental conditions that lead to an increase in the extracellular glutamate concentration induce a reduction of the *RRP* size without changing *Pr* at I synapses onto CA1-PCs.

To confirm that mGluRIII mediated the effects of DHK, we repeated the train stimulation and the integration analysis on IPSCs recorded at 0 mV in the continued presence of MSOP (100 μM), NBQX (10 μM), and APV (50 μM), before and after DHK (100 μM). Under these conditions, DHK did not change the *RRP* size, release probability, and refilling rate ($RRP_{DHK/Ctrl}$: 99% ± 14%, n = 7, p = 0.92; $Pr_{DHK/Ctrl}$: 150% ± 10%, p = 0.64; $R_{DHK/Ctrl}$: 88% ± 23%, p = 0.61; Figures 3H–3K). No change in the *RRP* size, release probability *Pr*, and refilling rate *R* was detected when DHK (100 μM) was applied in the continued presence of the mGluR7a antagonist MMPIP (10 μM), together with NBQX (10 μM) and APV (50 μm), suggesting that the effect of DHK is mostly mediated by mGluR7a receptors ($RRP_{DHK/Ctrl}$: 101% ± 11%, n = 10, p = 0.89; $Pr_{DHK/Ctrl}$: 101% ± 7%, p = 0.85; $R_{DHK/Ctrl}$: 94% ± 8%, p = 0.47; Figures 3L–3O). A similar reduction in the RRP size was evoked by the mGluR7a allosteric

(E) Cumulative IPSC amplitude normalized by the amplitude of the first IPSC in the train, plotted as a function of the stimulation timing, in control conditions (black) and in DHK (blue). Thick lines represent the linear fit of the last five IPSCs in each condition. The y-intercept of these lines was used to estimate the RRP.
(F) Mean and in-cell comparison of the effect of DHK on RRP, *Pr*, and R. The number of technical replicates was n = 15. The number of biological replicates was N = 5.
(G) Summary of the effect of DHK on RRP, *Pr*, and R, normalized by their values in control conditions.
(H–K) As in (D–G), for recordings obtained in the continued presence of the mGluRIII antagonist MSOP (100 μM). For (J), the number of technical replicates was n = 7. The number of biological replicates was N = 2.
(L–O) As in (D–G), for recordings obtained in the continued presence of the mGluR7a antagonist MMPIP (10 μM). For (N), the number of technical replicates was n = 10. The number of biological replicates was N = 3.
(P–S) As in (D–G), for recordings obtained in $[Ca^{2+}]_o$ = 2.5 mM. For (R), the number of technical replicates was n = 10. The number of biological replicates was N = 7. *p < 0.05, **p < 0.01, ***p < 0.001 by paired t test. Data are represented as mean ± SEM.

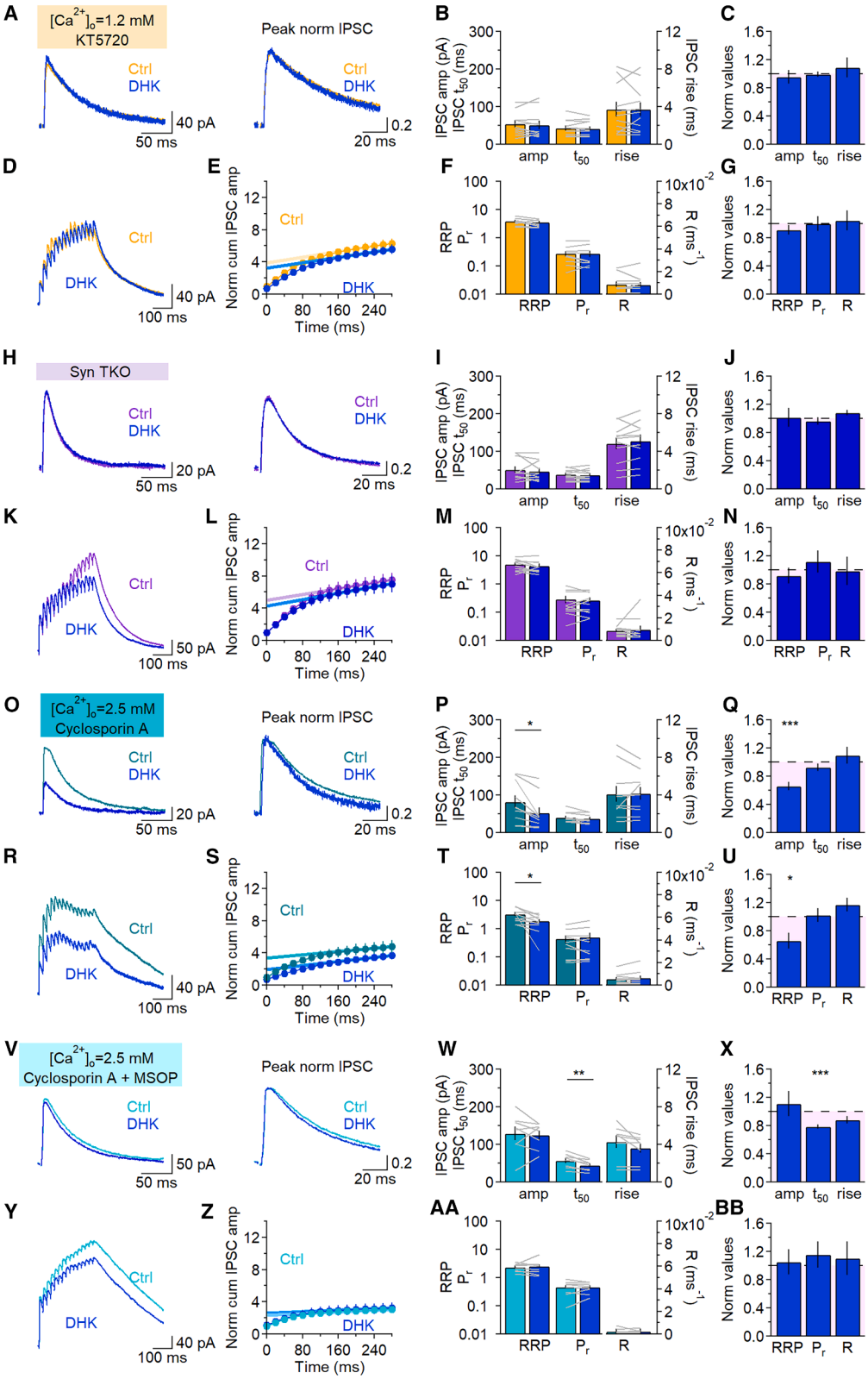

(legend on next page)

agonist CVN636 (1 μM), further supporting the idea that these receptors control the RRP size ($RRP_{CVN636/Ctrl}$: 74% ± 5%, n = 9, ***p = 5.7e−4; $Pr_{CVN636/Ctrl}$: 103% ± 8%, p = 0.75; $R_{CVN636/Ctrl}$: 98% ± 6%, p = 0.68; Figure S6). If mGluRIII did not change inhibition onto CA1-PCs in $\left[Ca^{2+}\right]_o$ = 2.5 mM, we would expect DHK not to induce any effect on *RRP*, *Pr*, or *R* in $\left[Ca^{2+}\right]_o$ = 2.5 mM. Consistent with this hypothesis, no effect of DHK was detected when $\left[Ca^{2+}\right]_o$ was increased from 1.2 to 2.5 mM ($RRP_{DHK/Ctrl}$: 88% ± 8%, n = 10, p = 0.17; $Pr_{DHK/Ctrl}$: 94% ± 15%, p = 0.68; $R_{DHK/Ctrl}$: 111% ± 22%, p = 0.64; Figures 3P–3S). Together, these findings suggest that mGluRIII activation limits inhibition onto CA1-PCs by reducing the *RRP* size at GABAergic axon terminals, an effect that only occurs when $\left[Ca^{2+}\right]_o$ is in the physiological range.

mGluRIII receptors reduce the RRP size by reducing PKA and synapsin activation

mGluRIII receptors are G-protein-coupled receptors linked to $G_{i/o}$ proteins. In addition to activating K^+ channels and inhibiting Ca^{2+} channels via liberation of $G_{\beta\gamma}$ subunits, they inhibit the membrane-associated enzyme adenylyl cyclase (AC).[13] By doing so, they reduce the intracellular concentration of cAMP and prevent the activation of protein kinase A (PKA). PKA, in turn, inhibits AC via a negative feedback loop (Figure S7).[37,38] At I synapses in the cerebellum, PKA inhibition can reduce the size of the *RRP* without altering the release probability *Pr* by changing the phosphorylation state of a family of vesicle-associated proteins called synapsins.[39–48] If PKA-dependent phosphorylation of synapsins is also critical to control the *RRP* size at I synapses onto CA1-PCs, then the mGluRIII-dependent suppression of inhibition should no longer be detected in the presence of a PKA inhibitor. To test this hypothesis, we recorded IPSCs at a holding potential of 0 mV in the presence of the PKA inhibitor KT5720 (1 μM), NBQX (10 μM), and APV (50 μM), before and after DHK (100 μM; Figures 4A–4G). KT5720 is an ATP-competitive antagonist for the ATP-binding site on the catalytic subunit of PKA.[49,50] This catalytic subunit must bind ATP before it can phosphorylate Ser/Thr residues on target proteins, so its blockade prevents the cAMP-dependent phosphorylation of PKA substrates.[51] Under these conditions, DHK did not change the IPSC amplitude or kinetics (amplitude: 95% ± 10%, n = 11, p = 0.65; t_{50}: 99% ± 3%, p = 0.85; rise: 109% ± 14%, p = 0.54; Figures 4A–4C) and did not induce any significant change in *RRP* size, *Pr* or the rate of vesicle replenishment of the RRP (*RRP*: 91% ± 6%, n = 11, p = 0.20; *Pr*: 100% ± 10%, p = 0.99; *R*: 105% ± 14%, p = 0.76; Figures 4D–4G). Similar results were also obtained when the IPSCs were recorded from SS1-PCs (Figure S8).

If the effects of DHK are mediated by PKA acting on synapsins, then DHK should also not change the IPSC amplitude and *RRP* size in slices from mice in which the genes encoding for synapsins I–III are deleted (here referred to as SynTKO; Figures 4H–4N). Consistent with this hypothesis, DHK (100 μM) did not change the IPSC amplitude or kinetics in CA1-PCs from SynTKO mice (amplitude: 102% ± 13%, n = 11, p = 0.91; t_{50}: 96% ± 5%, p = 0.53; rise: 108% ± 4%, p = 0.07; Figures 4H–4J). In SynTKO mice, DHK did not induce any significant change in *RRP* size, *Pr*, or *R* of I synapses (*RRP*: 92% ± 11%, n = 11, p = 0.50; *Pr*: 111% ± 16%, p = 0.47; *R*: 98% ± 20%, p = 0.93; Figures 4K–4N).

These findings indicate that mGluRIII activation at I synapses onto CA1-PCs reduces *RRP* through signaling cascades involving reduced PKA activation and reduced vesicle mobilization by synapsins. Given that the modulation of *RRP* at I synapses onto CA1-PCs is no longer detected at $\left[Ca^{2+}\right]_o$ = 2.5 mM, and *RRP* is smaller in 2.5 compared to 1.2 mM Ca^{2+} (**p = 2.1e−3; cf. Figures 3D–3G and 3P–3S), we wondered whether any signaling pathway that can change the net phosphorylation state of synapsins in a Ca^{2+}-dependent manner may be responsible for the lack of mGluRIII modulation of inhibition in $\left[Ca^{2+}\right]_o$ = 2.5 mM. Multiple protein kinases and phosphatases alter the phosphorylation state of synapsins,

Figure 4. PKA inhibition and synapsin loss prevent the spillover-induced reduction in the RRP at I synapses onto CA1-PCs

(A) Average IPSCs recorded with $\left[Ca^{2+}\right]_o$ = 1.2 mM in CA1-PCs, before (orange) and after DHK (100 μM; blue), in the continued presence of the PKA inhibitor KT5720 (1 μM). The traces on the right are normalized by the peak IPSC amplitude.

(B) Summary of the effect of DHK on the IPSC amplitude and kinetics in KT5720.

(C) Summary of the relative change in IPSC amplitude and kinetics induced by DHK applied in the continued presence of KT5720.

(D) Representative IPSC train recorded in response to *stratum radiatum* stimulation with 15 pulses at 50 Hz (280 ms), before (orange) and after DHK (blue), in the continued presence of KT5720 and in $\left[Ca^{2+}\right]_o$ = 1.2 mM.

(E) Cumulative IPSC amplitude normalized by the amplitude of the first IPSC in the train, plotted as a function of the stimulation timing, in control conditions (orange) and in DHK (blue). Thick lines represent the linear fit of the last five IPSCs in each condition. The y-intercept of these lines was used to estimate the RRP.

(F) Mean and in-cell comparison of the effect of DHK on RRP, Pr, and R, when applied in the presence of KT5720.

(G) Summary of the effect of DHK on RRP, Pr, and R, when applied in the continued presence of KT5720. The data were normalized by their values in control conditions.

(H–N) As in (A–G), for data collected from CA1-PCs in Syn TKO mice, in control conditions (purple) and in the presence of DHK (blue).

(O–U) As in (A–G), for data collected with $\left[Ca^{2+}\right]_o$ = 2.5 mM and in the continued presence of the calcineurin inhibitor cyclosporin A (1 μM), in control conditions (teal) and in the presence of DHK (blue).

(V–BB) As in (A–G), for data collected with $\left[Ca^{2+}\right]_o$ = 2.5 mM and in the continued presence of the calcineurin inhibitor cyclosporin A (1 μM) and the mGluRIII antagonist MSOP (100 μM), in control conditions (cyan) and in the presence of DHK (blue). For (A–G), the number of technical replicates was n = 11. The number of biological replicates was N = 6. For (H–N), the number of technical replicates was n = 11. The number of biological replicates was N = 6. For (O–U), the number of technical replicates was n = 10. The number of biological replicates was N = 8. For (V–BB), the number of technical replicates was n = 8. The number of biological replicates was N = 4. *p < 0.05, **p < 0.01, and ***p < 0.001 by paired t test. Data are represented as mean ± SEM.

including MAP kinase,[52–54] CdK5,[55–57] CaMKII,[53,54,58,59] and PP2A/PP1[53,58] (Figure S7). Out of all these molecules, CaMKII is expressed at very low levels in INs,[60,61] and although MAP kinase can be activated by Ca^{2+}, its increased activity would not explain the reduced *RRP* in 2.5 mM $[Ca^{2+}]_o$. CdK5 and PP2A/PP1 are not modulated by $[Ca^{2+}]_o$. By contrast, the protein phosphatase PP2B (i.e., calcineurin) is a ubiquitous Ser/Thr phosphatase activated by elevated Ca^{2+} levels and subsequent activation of calmodulin.[62] Calcineurin is known to dephosphorylate synapsins and antagonize the effect of MAP kinase and CdK5 on these molecules.[53,63] Therefore, if the reduced *RRP* in $\left[Ca^{2+}\right]_o$ = 2.5 mM is due to synapsins dephosphorylation by calcineurin, we would expect cyclosporin A (1 μM), an inhibitor of calcineurin, to increase the *RRP* and rescue its modulation by DHK in 2.5 mM $[Ca^{2+}]_o$. To test this hypothesis, we repeated our single and train stimulation in slices incubated with cyclosporin A (1 μM) for 30–60 min (Figures 4O–4U). IPSCs were recorded in cells voltage clamped at 0 mV, in the presence of cyclosporin A (1 μM), NBQX (10 μM), and APV (50 μM). Consistent with our hypothesis, DHK (100 μM) reduced the IPSC amplitude (***p = 3.7e−4; Figures 4O–4Q) and the *RRP* in $\left[Ca^{2+}\right]_o$ = 2.5 mM in the presence of cyclosporin A (*p = 0.01; Figures 4R–4U). The findings that (1) DHK reduced the IPSC amplitude and *RRP* in slices maintained in cyclosporin A and $\left[Ca^{2+}\right]_o$ = 2.5 mM (Figures 4O–4U) and that (2) the effect of DHK was no longer detectable in slices maintained in cyclosporin A and MSOP in $\left[Ca^{2+}\right]_o$ = 2.5 mM (Figures 4V–4BB) indicate that the inability to detect an mGluRIII-dependent reduction of inhibition onto CA1-PCs in $\left[Ca^{2+}\right]_o$ = 2.5 mM is likely due to an altered balance in the phosphorylation state of synapsins mediated by calcineurin.

mGluRIII receptors reduce proximal and distal inhibition onto CA1-PCs

The EM data in Figure 1 show that mGluRIII is expressed at proximal and distal I synapses onto CA1-PCs, which are mostly formed by PV- and SST-INs, respectively. To selectively activate I-afferents from PV- or SST-INs and determine whether these largely non-overlapping inputs are equally susceptible to glutamate uptake blockade, we performed stereotaxic injections of a floxed viral construct encoding ChR2 in $Pvalb^{Cre/+}$ and $Sst^{Cre/+}$ mice (Figure 5A). We then recorded optically evoked IPSCs (oIPSCs) in CA1-PCs. DHK reduced the amplitude of oIPSCs from PV-INs to 74% ± 8% (n = 10; *p = 0.01; Figures 5B–5E) and that of oIPSCs from SST-INs to 74% ± 4% (n = 10; ***p = 7.9e−5; Figures 5F–5I). Given the different spatial distribution of PV and SST inputs onto the dendritic tree of CA1-PCs (Figure 5J), inhibition from these two different classes of INs is prone to different levels of electrotonic attenuation, as the synaptic currents propagate toward the soma (Figure S9). Accordingly, cable theory suggests that with somatic voltage-clamp recordings, fast currents arising at a distance from the soma are attenuated more than currents with slower kinetics arising in more proximal compartments.[64] This would suggest that glutamate spillover could induce a larger reduction of distal compared to proximal inhibition. We tested this hypothesis using a compartmental model that reproduced not only the realistic morphology of CA1-PCs but also the voltage escape associated with somatic voltage-clamp recordings[65,66] (Figures S9A–S9D). We constrained the synaptic weight of PV inputs in the model (w_{PV} = 485 pS) to ensure that it would generate somatic mIPSCs, at 0 mV, with similar amplitude and kinetics compared to those recorded experimentally (Figures 3A–3D; Figure S9E). The synaptic weight of SST inputs was set to be the same (w_{PV} = w_{SST} = 485 pS). The release probability of PV-INs was set to Pr_{PV} = 0.10 in $\left[Ca^{2+}\right]_o$ = 1.2 mM, a value we derived using a power-law relationship from a starting value of Pr_{PV} = 0.8 measured in $\left[Ca^{2+}\right]_o$ = 2.0 mM[19,67,68] (Figure S9F). The model showed that evoking GABA release from 4 out of 40 PV inputs generated somatic oIPSCs with the same amplitude and kinetics of the PV-oIPSCs recorded experimentally (Figure 5K, top). Based on three-dimensional (3D) EM reconstructions, the number of SST inputs onto CA1-PCs is 8.3 times larger than that of PV-INs (i.e., 40 × 8.3 = 332).[69] Assuming that all these terminals are activated synchronously by the full-field light stimulus in our optogenetics experiments and given that oIPSCs similar to those detected experimentally could be generated by evoking release from 18 SST inputs in the model (Figure 5K, bottom), we estimated the release probability of SST-INs to be Pr_{SST} = 18/332 = 0.05 (Figure S9F). Based on the data shown in Figure 3, promoting glutamate spillover reduces the size of the *RRP*, which is composed of N release sites. Our simulations showed that a 25%–28% reduction in the amplitude of somatically recorded PV- or SST-oIPSCs (Figures 5E and 5I) could be obtained by reducing the total number of PV release sites from 40 to 30 and that of SST-INs from 332 to 260. This is analogous to reducing the number of active release sites of PV-INs from 4 to 3 and of SST-INs from 18 to 13, representing a 25% and 28% reduction, respectively. Therefore, experimental conditions that promote glutamate spillover and mGluRIII activation induce minimal—if any—change in the relative strength of proximal versus distal inhibition onto CA1-PCs (Figure 5L). The relevance of this effect in the context of intact networks and encoding of spatial information in CA1-PCs is analyzed below.

mGluRIII receptors increase the accuracy of space representation by CA1-PCs

The *in vitro* experiments described above indicate that mGluRIII modulates synaptic transmission in area CA1, limiting excitation and inhibition onto CA1-INs and reducing inhibition, but not excitation, onto CA1-PCs under physiological $\left[Ca^{2+}\right]_o$ conditions. Since CA1-PCs are crucial for encoding spatial representations, and the influence of mGluRIII on these representations has not been previously explored, we conducted a series of *in vivo* experiments to investigate these phenomena. In these experiments, we performed simultaneous whole-cell patch-clamp recordings from CA1-PCs using a biocytin-containing internal solution (0.2%) and extracellular local field potential (LFP) recordings in area CA1 (Figure 6A, top). The glass electrode used to record the local field potential also contained either the mGluRIII antagonist MSOP (100 μM) or a vehicle solution. *Post*

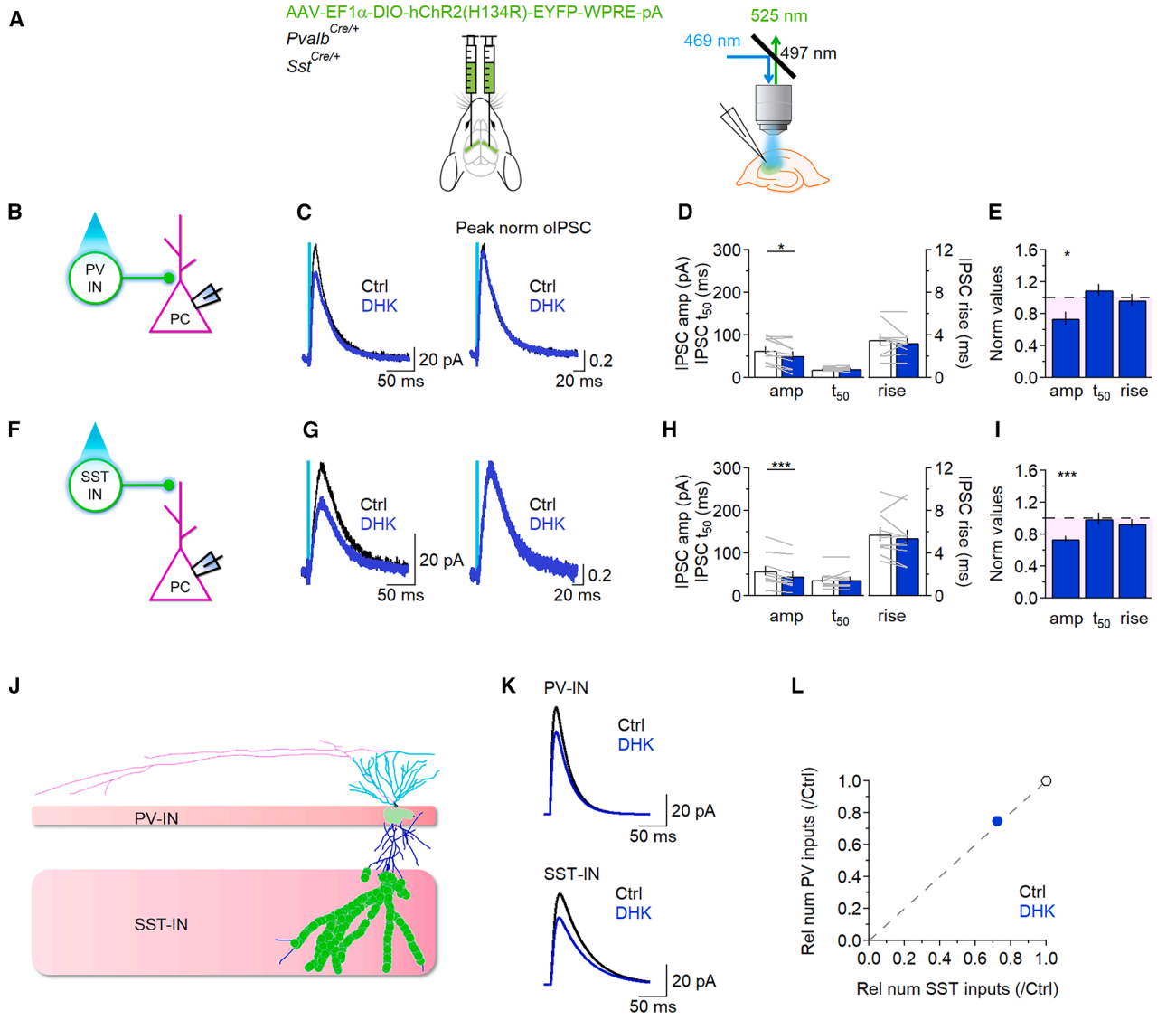

Figure 5. Proximal and distal inhibition onto CA1-PCs is modulated by mGluRIII

(A) Schematic representation of the stereotaxic injections of viral constructs encoding ChR2 in hippocampal area CA1 of *Pvalb*$^{Cre/+}$ and *Sst*$^{Cre/+}$ mice and of the experiment settings.

(B) Scheme describing optogenetic activation of PV-INs.

(C) oIPSCs evoked by optical stimulation of PV-INs before (black) and after DHK (100 μM; blue). The traces on the right are normalized by the oIPSC peak.

(D) Summary of the effect of DHK on the oIPSC amplitude and kinetics, in *Pvalb*$^{Cre/+}$ mice.

(E) Summary of the effect of DHK on the oIPSC amplitude and kinetics, normalized by their values in control conditions.

(F–I) As in (B–E), for oIPSCs evoked by optical stimulation of SST-INs.

(J) Morphology of CA1-PCs receiving PV inputs onto the soma and the proximal portion of the apical dendrite (0–50 μm; light green dots) or SST inputs onto the distal portion of the apical dendrite (>200 μm; green dots).

(K) Example of oIPSCs generated with a compartmental model of a CA1-PC in response to activation of PV (top) or SST inputs (bottom). The model reproduces the effect of DHK on the amplitude and kinetics of these events detected experimentally (C and G).

(L) A 25%–28% reduction in the amplitude of the oIPSC recorded at the soma can be obtained by reducing the number of active PV-inputs from 4 to 3 and that of SST-inputs from 11 to 8. The scatterplot shows these results as relative effects in control conditions (black) and in DHK (blue). For (C–E), the number of technical replicates was $n = 10$. The number of biological replicates was $N = 4$. For (F–I), the number of technical replicates was $n = 10$. The number of biological replicates was $N = 6$. $^{*}p < 0.05$, $^{**}p < 0.01$, and $^{***}p < 0.001$ by paired t test. Data are represented as mean ± SEM.

hoc analysis of the solution's spatial spread (~500 μm) was performed by replacing the LFP electrode with a new electrode containing SR-101 (1 mM), a fluorescent dye selectively taken up by astrocytes (Figure 6A, bottom; see Methods). In anesthetized mice, MSOP depolarized V_m and increased the action potential frequency ($n = 10$, slow V_m $^{*}p = 0.01$, action potential frequency

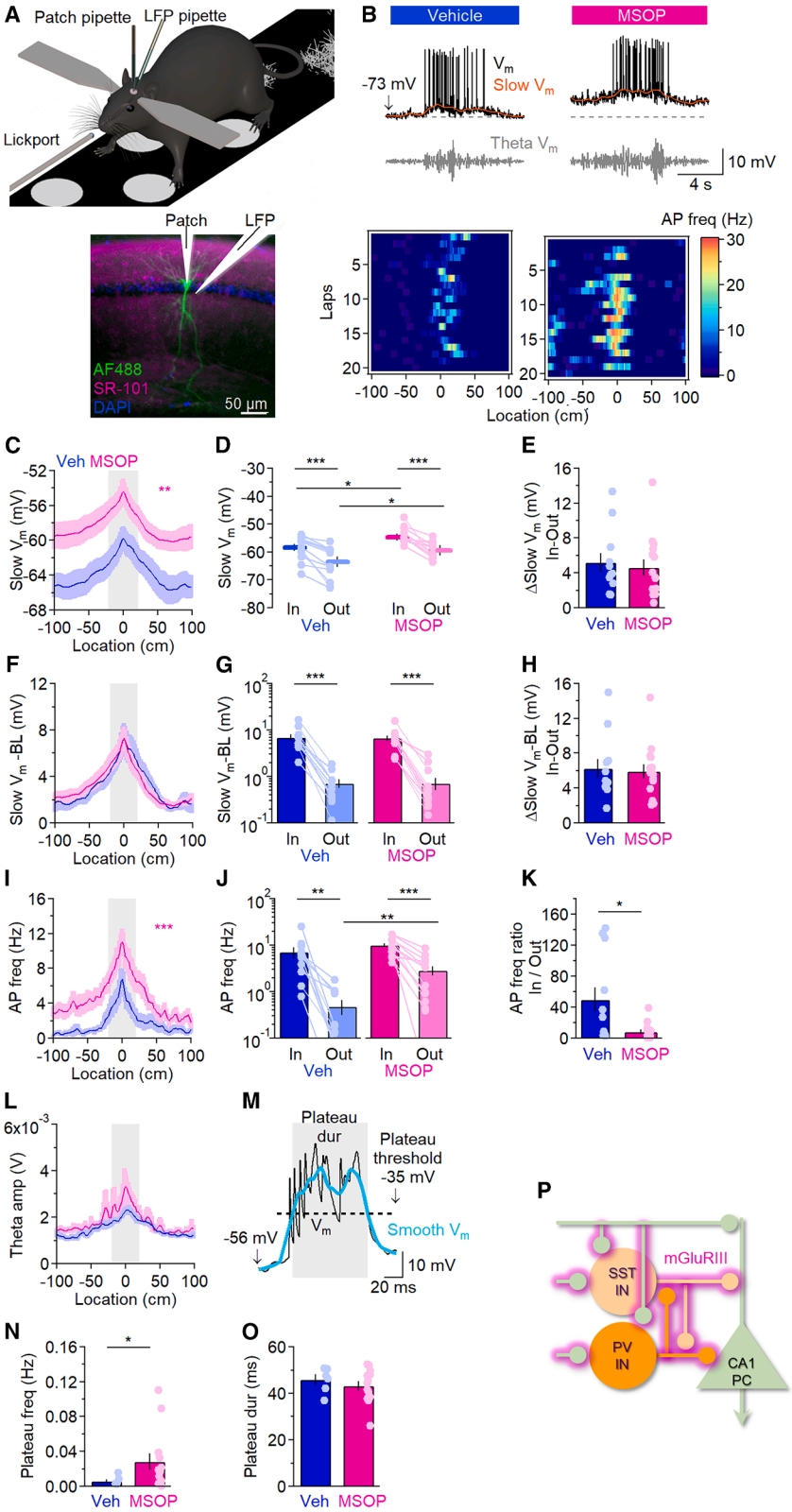

(legend on next page)

*p = 0.03; Figure S10). To examine how mGluRIII shapes the activity of CA1 place cells in awake-behaving mice, we obtained current-clamp, whole-cell patch-clamp recordings from CA1 place cells in mice trained to run on a linear treadmill for a 10% sucrose reward (n = 12 in vehicle; n = 15 in MSOP; Figure 6A). The recordings included both pre-existing place cells (n = 4 in vehicle; n = 9 in MSOP) and silent cells, which were experimentally induced to form place fields using the behavioral timescale plasticity (BTSP) protocol (n = 8 in vehicle; n = 6 in MSOP).[70] The intracellular V_m dynamics were decomposed into three components: suprathreshold action potential firing, a slow subthreshold V_m component (<2 Hz), and an intracellular theta oscillation component (5–10 Hz; Figure 6B). Consistent with prior work,[71] vehicle-treated CA1 place cells showed a ramp-like depolarization in the slow V_m, a place-specific increase in action potential firing rate, and increased theta oscillation amplitude (Figure 6B). Compared to these cells, CA1 place cells in the MSOP-treated group exhibited a ~5 mV position-independent depolarizing shift in the slow V_m (Figures 6C–6H). However, the width of the subthreshold ramp (i.e., the distance along the track over which the slow V_m remained within 20% of its peak value) was not altered by MSOP (Figures 6F–6H; Figure S11A, p = 0.59). For this reason, in the remainder of the analysis (Figures 6D, 6E, 6G, 6H, 6J, and 6K), we defined the in-field region as the distance spanning 20 cm before and after the peak of the slow V_m.

The ~5 mV depolarization induced by MSOP resulted in a significantly increased out-of-field firing rate (Figures 6I and 6J) and a corresponding decrease in the ratio of in-field to out-of-field firing (*p = 0.02; Figure 6K). Consistent with the change in firing patterns, the place field size, defined as the distance over which the action potential firing rate exceeded 20% of its peak value, was increased in the presence of MSOP (Figures S11B and S11C). The spatial information content of place cells (bits per spike) was significantly reduced, while the place field sparsity was increased in MSOP (Figures S11D and S11E). Importantly, these effects were not attributable to changes in place field stability across laps, which did not differ between vehicle and MSOP conditions (Figure S11F). In addition, the intracellular theta oscillation amplitude remained unchanged (p = 0.15; Figure 6L). These findings indicate that the observed changes in place cell firing largely reflect the MSOP-induced V_m depolarization. Consistent with this interpretation, CA1 place cells with comparable baseline V_m exhibited similar ramp depolarization and firing rates in vehicle and MSOP conditions (depolarization p = 0.09; firing rate: p = 0.16; Figure S12). To further explore these effects, we analyzed complex spike bursts, or "plateaus," which are mediated by dendritic plateau potentials (i.e., large voltage events initiated in the distal dendrites of CA1-PCs)[70,72,73] (Figure 6M). MSOP increased plateau frequency but did not affect plateau duration (frequency: *p = 0.03; duration: p = 0.41; Figures 6N and 6O). A schematic representation of the presynaptic sites of mGluRIII-dependent modulation of neurotransmitter release is shown in Figure 6P. If mGluRIII activation *in vivo* is driven by glutamate spillover, we would expect the effects of MSOP to resemble those observed when extracellular diffusion is reduced using dextran (1 mM).[74,75] Consistent with this prediction, dextran produced similar effects on V_m dynamics and spatial selectivity as MSOP (Figures S13 and S11). Together, these results suggest that spillover-mediated mGluRIII activation is critical for encoding spatial information in CA1 place cells. The observed effects are consistent with mGluRIII activation, causing a net increase in synaptic inhibition of CA1 place cells *in vivo*.

DISCUSSION

The main finding in this work is that, under experimental conditions that closely match the physiological Ca^{2+} concentration in the cerebrospinal fluid[18] and promote mGluRIII activation, there is no target-cell-specific control of inhibition onto CA1-PCs. The same experimental conditions, however, lead to reduced excitation onto CA1-INs but not PCs. These results differ, in part, from those collected in slice physiology experiments performed using a higher extracellular $\left[Ca^{2+}\right]_o$, which showed that mGluRIII reduces excitation and inhibition onto CA1-INs, not CA1-PCs.[3,16,24,76] We identify PKA-dependent

Figure 6. Spillover-mediated mGluRIII activation reduces place field formation and strength

(A) Top: schematic of the linear treadmill and recording apparatus for the *in vivo* electrophysiology experiments. Bottom: confocal image of biocytin-filled CA1-PCs (green), SR-101 (1 mM) astrocyte labeling to depict the area affected by MSOP/vehicle (magenta), and DAPI (blue) in a section of the mouse hippocampus.

(B) Example of raw V_m (black), low-pass filtered V_m (slow V_m; orange), and theta-filtered intracellular V_m (gray) for CA1-PC place cells recorded in vehicle and MSOP. The heatmaps represent the spatial action potential (AP) firing rate of these cells shown for 20 consecutive laps. The dashed line marks −73 mV.

(C) Mean spatially binned slow V_m ramp map, calculated across all CA1 place cells recorded. The gray shaded area represents the location of the maximum in-field region, used for (D and E).

(D and E) Quantification of the maximum in-field, minimum out-of-field V_m ramp values (D), and their difference (E). MSOP depolarizes the slow V_m by ~5 mV.

(F–H) As in (C–E), but for baseline (BL) V_m-subtracted slow V_m, showing no change in the absolute amplitude of the slow V_m ramp depolarization between vehicle and MSOP.

(I and J) As in (C and D) but for action potential frequency.

(K) Ratio of maximum versus minimum action potential frequency. MSOP decreases this ratio.

(L) Mean spatially binned intracellular theta envelope map, calculated across all CA1 place cells recorded.

(M) Example of raw V_m (black) and smoothed, subthreshold V_m (cyan) during a spontaneous plateau. The gray shaded area represents the duration of the plateau, calculated from the threshold value of −35 mV.

(N and O) Summary graphs of the plateau frequency and duration, respectively. MSOP increased the plateau frequency without altering the plateau duration.

(P) Diagram of hippocampal connectivity and synaptic location of mGluRIII-dependent modulation. The number of technical replicates was n = 12 for vehicle and n = 15 for MSOP. The number of biological replicates was N = 9 for vehicle and N = 10 for MSOP, respectively. *p < 0.05, **p < 0.01, ***p < 0.001 by GEE for panels (C, F, I, and L). *p < 0.05, **p < 0.01, ***p < 0.001 by GEE followed by paired or unpaired t test for panels D, G, J. *p < 0.05, **p < 0.01, ***p < 0.001 by unpaired t test for panels E, H, K, N, O. Data are represented as mean ± SEM.

phosphorylation of synapsins as a key mechanism that limits the inhibition of CA1-PCs by reducing the size of the RRP. A key question is how increasing $\left[Ca^{2+}\right]_o$ prevents the mGluRIII-dependent modulation of synaptic inhibition of CA1-PCs. Our experimental data show that varying $\left[Ca^{2+}\right]_o$ alters the activation of the Ca^{2+}-dependent phosphatase calcineurin, which can dephosphorylate synapsins. We speculate that, at high $\left[Ca^{2+}\right]_o$, synapsins may be in a net dephosphorylated state due to the presence of high-affinity, Ca^{2+}-dependent phosphatases in the bouton.[77] Therefore, we propose that varying $[Ca]_o^{2+}$ can modify the mGluRIII-dependent control of inhibition onto CA1-PCs by altering the phosphorylation state of proteins like synapsins, which are involved in regulating the *RRP*.

We do not know why the mGluRIII-dependent modulation of inhibition onto CA1-PCs is sensitive to $\left[Ca^{2+}\right]_o$ but excitation is not. We acknowledge that synapsins have unique functions at excitatory versus inhibitory synapses. At excitatory synapses, synapsins maintain the reserve pool of glutamatergic vesicles, whereas at inhibitory synapses they regulate the size of the RRP.[78] However, there is currently no indication that the biophysical properties of these proteins differ across pre-synaptic terminals onto different cell types, making this an unlikely scenario. Our ultrastructural analysis shows that one mGluRIII type—mGluR7a—is more abundant at I compared to E terminals, but we do not know whether target-cell-specific differences in the localization of mGluRIII relative to the RRP or to other proteins implicated with the complex regulatory pathway that controls RRP size exist. These ultrastructural features, as well as higher levels of cross-talk between E–I and E–E synapses, and differences in calcium buffering capacities at E/I synapses, could all contribute to the higher $\left[Ca^{2+}\right]_o$-sensitivity of inhibition compared to excitation onto CA1-PCs.[79] There is, in fact, anatomical data showing that the distance between glutamatergic and GABAergic synapses could be even smaller than that between glutamatergic synapses, with finer estimates emerging from the use of cryo-EM approaches.[80–82] Target-cell-specific differences in the ability of activity-dependent retrograde signals to control GABA release could make the scenario even more complex.[83,84]

The finding that the effects of mGluRIII activation are mediated by PKA inhibition and dephosphorylation of its vesicle-associated target proteins, synapsins, is reminiscent of the signaling pathways that regulate the occupancy of the *RRP* at E synapses in the cerebellum, suggesting that this regulatory pathway may be widespread across E/I synapses across the brain.[39] Our data show that an mGluRIII-dependent control of inhibition onto principal cells occurs in SS1. An essential finding of this work, however, is that it identifies mGluRIII as a family of receptors capable of inhibiting the PKA-synapsin signaling pathway, leading to a reduction in *RRP*. PKA may not be the only protein implicated with regulating the phosphorylation state of synapsins, as there are multiple protein kinases and phosphatases known to control the phosphorylation state of these molecules.[52–59] However, the fact that blocking PKA activity prevents the reduction of inhibition onto CA1-PCs in the presence of DHK suggests PKA is a key player in this regulatory mechanism.

The inability to detect an mGluRIII-dependent modulation of GABA release onto CA1-PCs in the absence of glutamate transporter blockers *in vitro* but not *in vivo* is consistent with different levels of ongoing synaptic activity in living organisms and with the fact that many glutamatergic afferents to the hippocampus are resected during slice preparation. This finding also implies that mGluRIII may control the excitability of CA1-PCs in an activity-dependent manner, reducing it at increasing activity levels of excitatory networks. In this case, one could ask whether there is any potential therapeutic benefit of using mGluRIII antagonists to dampen epileptic seizures or cognitive dysfunction in diseases associated with increased extracellular glutamate levels, like Alzheimer disease. A reduced expression of mGluRII/III has been detected in human Ammon's horn sclerosis[85] and the pilocarpine-induced *status epilepticus* model of chronic epilepsy in rodents.[86–89] However, the use of mGluRIII agonists has shown mixed responses in animal models of epilepsy. Some groups reported that the mGluRIII agonists, L-AP4 and L-SOP, are proconvulsive, and mGluRIII antagonists like MCPA are anticonvulsive.[90] Others showed that mGluRIII agonists are anticonvulsants in generalized motor and focal seizures[91–100] and that other antagonists, such as MAP4 and MPPG, are proconvulsant.[90,93] A probable reason for the discrepancy of these results may lie in the limited specificity of the pharmacological tools used to modulate mGluRIII receptors and in the heterogeneous mGluRIII expression and recruitment at different synapses throughout the hippocampal circuitry and in different epilepsy models, making the results particularly challenging to interpret.

The *in vivo* experiments underscore a pivotal role for mGluRIII-mediated synaptic modulation in shaping spatial representations in hippocampal area CA1 and significantly extend our current understanding of the role of mGluRIII for behaviorally relevant neural circuit dynamics. The impact of mGluRIII modulation was evident even without pharmacological manipulations, such as glutamate uptake blockade, indicating that the *in vivo* environment provides sufficient glutamate spillover to activate these receptors. This highlights the complementary role of studying synaptic transmission in slices and within intact networks, where ongoing neural activity reveals physiological mechanisms that may be obscured in reduced preparations.

We observed that mGluRIII activation has effects consistent with an overall increased level of synaptic inhibition, thus altering the spatially tuned firing patterns of individual CA1-PCs and enhancing the CA1 network's ability to sparsely encode spatial information. Our findings align with prior *in vivo* work highlighting the critical role of inhibition in maintaining flexible and selective coding of CA1 place cells while adding to these results by demonstrating that mGluRIII activation plays a role in modulating inhibition.[101–103] Specifically, mGluRIII activation appears to also affect distal GABAergic inhibition onto CA1-PCs, as evidenced by the increased frequency of dendritically driven plateaus following the mGluRIII blockade.

Based on our *in vitro* recordings, we hypothesize that the observed mGluRIII-mediated increase in net synaptic inhibition

of CA1-PCs is the result of a combination of reduced excitation of disinhibitory CA1-INs and reduced activation of IN-to-IN synapses. Both effects would enhance PV- and SST-IN activity, thereby exerting a net suppressive effect on CA1-PC activity *in vivo*. The potential behavioral implications of these findings are profound. By modulating the E/I ratio in the CA1 circuit, mGluRIII would be well positioned to influence the accuracy and stability of spatial representations in CA1. This modulation may play a critical role in adaptive navigation and spatial memory formation, potentially enabling dynamic adjustments to the E/I balance necessary to encode new environments while preserving established spatial maps. Such flexibility is thought to be essential for effective learning and memory processes,[104] underscoring the functional relevance of mGluRIII receptors in hippocampal circuit dynamics.

Limitations of the study

The EM studies included in this work rely on the analysis of 2D images, not 3D reconstructions. Although 3D analysis provides a more complete description of the ultrastructure of the hippocampal neuropil, we do not think that this biases our estimates of the subcellular distribution of different mGluRIII types. mGluRIII receptors are composed of three main receptor types (mGluR4, mGluR7, and mGluR8 in the hippocampus). Although our *in vitro* findings indicate that mGluR7 is mostly responsible for the effects we describe, we did not validate this finding *in vivo*, and we also did not analyze the specific contribution of mGluR4 and mGluR8 for lack of specific pharmacological agents. The use of specific BAC transgenic mouse lines might help address this, if loss of these receptors is not associated with compensatory changes in the expression or spatial distribution of other mGluRIII types. We tested the effect of mGluRIII activation in two populations of interneurons (PV- and SST-INs), even though other types of hippocampal INs may also be involved in shaping place field activity. Future studies will be useful to address this potential limitation. Finally, there are two potential limitations for the *in vivo* experiments. First, the use of MSOP *in vivo* is not used to selectively block spillover-activated presynaptic mGluRIII receptors. Our goal with this manipulation was simply to assess the overall effect of mGluRIII activation on place field activity. Second, dextran alters extracellular diffusion of all neurotransmitters, not only glutamate. Even in this case, our goal was to assess the net effect of neurotransmitter spillover in shaping processing of spatial information. In principle, these concerns could be addressed by using methods that are more selective for either presynaptic mGluRIII or glutamate diffusion. In practice, to the best of our knowledge, these methods do not currently exist.

RESOURCE AVAILABILITY

Lead contact

Further information and requests for resources and reagents should be directed to and will be fulfilled by the lead contact, Dr. Annalisa Scimemi (scimemia@gmail.com).

Materials availability

No new materials have been generated in this study.

Data and code availability

- All primary data used in this work and complete statistical analyses for each figure have been deposited in an Open Science Framework repository (https://osf.io/ucj2d/).
- All files pertaining to the NEURON simulations were uploaded to the ModelDB database (https://modeldb.science/). Additional details can be found in our GitHub repository (https://github.com/scimemia/mGluRIII) and on Zenodo (https://doi.org/10.5281/zenodo.19455971).
- All original code is publicly available from the lead contact as of the date of publication. Any additional information required to reanalyze the data reported in this paper is available from the lead contact upon request.

STAR★METHODS

Detailed methods are provided in the online version of this paper and include the following:

- KEY RESOURCES TABLE
- EXPERIMENTAL MODEL AND STUDY PARTICIPANT DETAILS
  - Mice
- METHOD DETAILS
  - Stereotaxic intracranial AAV injections
  - Acute slice preparation
  - *In vitro* electrophysiology recordings and optogenetics
  - Surgeries for *in vivo* electrophysiology experiments and training
  - Behavioral setup
  - *In vivo* electrophysiology
  - Histology
  - Antibodies
  - Tissue collection and pre-embedding immunolabeling for EM analysis
  - NEURON model of CA1-PCs
  - EM analysis
  - *In vitro* electrophysiology analysis
  - *In vivo* electrophysiology and behavior analysis
- QUANTIFICATION AND STATISTICAL ANALYSIS

ACKNOWLEDGMENTS

We would like to thank Drs. P.J. Albrecht and G.C. Todd for mouse colony management and genotyping and T.R. Buddhavarapu for technical support. Special thanks to Prof. D. M. Kullmann for invaluable comments on this manuscript and Prof. B. L. Sabatini for discussions. The funding sources are as follows: National Institutes of Health grants R56NS129556 and R56NS140423 (C.G., F.C., and A.S.), National Science Foundation grant IOS2011998 (A.S.), and Smith Family Awards Program for Excellence in Biomedical Research (C.G.). Images were acquired using an EVIDENT VS200 Slide Scanner funded by the National Institutes of Health S10 SIG grant (S10OD036207; A.S.).

AUTHOR CONTRIBUTIONS

Conceptualization, C.G., F.C., and A.S.; data curation, M.A.P., M.M., N.D., C.G., and A.S.; formal analysis, M.A.P., M.M., N.D., and A.S.; funding acquisition, C.G., F.C., and A.S.; investigation, M.A.P., M.M., T.J.R., and A.S.; methodology, N.D., C.G., and A.S.; project administration, A.S.; resources, C.G., F.C., and A.S.; software, M.A.P., N.D., C.G., and A.S.; supervision, C.G., F.C., and A.S.; validation, M.M. and A.S.; visualization, M.A.P., M.M., and A.S.; writing – original draft, M.M., C.G., F.C., and A.S.; writing – review and editing, C.G., F.C., and A.S.

DECLARATION OF INTERESTS

The authors declare no competing interests.

SUPPLEMENTAL INFORMATION

Supplemental information can be found online at https://doi.org/10.1016/j.celrep.2026.117388.

Received: March 5, 2025
Revised: March 16, 2026
Accepted: April 21, 2026
Published: May 28, 2026

REFERENCES

1. Pelkey, K.A., Chittajallu, R., Craig, M.T., Tricoire, L., Wester, J.C., and McBain, C.J. (2017). Hippocampal GABAergic Inhibitory Interneurons. Physiol. Rev. *97*, 1619–1747. https://doi.org/10.1152/physrev.00007.2017.
2. Vignes, M., Clarke, V.R., Davies, C.H., Chambers, A., Jane, D.E., Watkins, J.C., and Collingridge, G.L. (1995). Pharmacological evidence for an involvement of group II and group III mGluRs in the presynaptic regulation of excitatory synaptic responses in the CA1 region of rat hippocampal slices. Neuropharmacology *34*, 973–982. https://doi.org/10.1016/0028-3908(95)00093-l.
3. Scanziani, M., Gähwiler, B.H., and Charpak, S. (1998). Target cell-specific modulation of transmitter release at terminals from a single axon. Proc. Natl. Acad. Sci. USA *95*, 12004–12009. https://doi.org/10.1073/pnas.95.20.12004.
4. Gereau, R.W., 4th, and Conn, P.J. (1995). Multiple presynaptic metabotropic glutamate receptors modulate excitatory and inhibitory synaptic transmission in hippocampal area CA1. J. Neurosci. *15*, 6879–6889.
5. Gereau, R.W., 4th, and Conn, P.J. (1995). Roles of specific metabotropic glutamate receptor subtypes in regulation of hippocampal CA1 pyramidal cell excitability. J. Neurophysiol. *74*, 122–129. https://doi.org/10.1152/jn.1995.74.1.122.
6. Desai, M.A., McBain, C.J., Kauer, J.A., and Conn, P.J. (1994). Metabotropic glutamate receptor-induced disinhibition is mediated by reduced transmission at excitatory synapses onto interneurons and inhibitory synapses onto pyramidal cells. Neurosci. Lett. *181*, 78–82. https://doi.org/10.1016/0304-3940(94)90564-9.
7. Baskys, A., and Malenka, R.C. (1991). Agonists at metabotropic glutamate receptors presynaptically inhibit EPSCs in neonatal rat hippocampus. J. Physiol. *444*, 687–701. https://doi.org/10.1113/jphysiol.1991.sp018901.
8. Kogo, N., Dalezios, Y., Capogna, M., Ferraguti, F., Shigemoto, R., and Somogyi, P. (2004). Depression of GABAergic input to identified hippocampal neurons by group III metabotropic glutamate receptors in the rat. Eur. J. Neurosci. *19*, 2727–2740. https://doi.org/10.1111/j.0953-816X.2004.03394.x.
9. Bradley, S.R., Levey, A.I., Hersch, S.M., and Conn, P.J. (1996). Immunocytochemical localization of group III metabotropic glutamate receptors in the hippocampus with subtype-specific antibodies. J. Neurosci. *16*, 2044–2056.
10. Shigemoto, R., Kinoshita, A., Wada, E., Nomura, S., Ohishi, H., Takada, M., Flor, P.J., Neki, A., Abe, T., Nakanishi, S., and Mizuno, N. (1997). Differential presynaptic localization of metabotropic glutamate receptor subtypes in the rat hippocampus. J. Neurosci. *17*, 7503–7522.
11. Shigemoto, R., Kulik, A., Roberts, J.D., Ohishi, H., Nusser, Z., Kaneko, T., and Somogyi, P. (1996). Target-cell-specific concentration of a metabotropic glutamate receptor in the presynaptic active zone. Nature *381*, 523–525. https://doi.org/10.1038/381523a0.
12. Corti, C., Aldegheri, L., Somogyi, P., and Ferraguti, F. (2002). Distribution and synaptic localisation of the metabotropic glutamate receptor 4 (mGluR4) in the rodent CNS. Neuroscience *110*, 403–420. https://doi.org/10.1016/s0306-4522(01)00591-7.
13. Niswender, C.M., and Conn, P.J. (2010). Metabotropic glutamate receptors: physiology, pharmacology, and disease. Annu. Rev. Pharmacol. Toxicol. *50*, 295–322. https://doi.org/10.1146/annurev.pharmtox.011008.145533.
14. Conn, P.J., and Pin, J.P. (1997). Pharmacology and functions of metabotropic glutamate receptors. Annu. Rev. Pharmacol. Toxicol. *37*, 205–237. https://doi.org/10.1146/annurev.pharmtox.37.1.205.
15. Bradley, S.R., Rees, H.D., Yi, H., Levey, A.I., and Conn, P.J. (1998). Distribution and developmental regulation of metabotropic glutamate receptor 7a in rat brain. J. Neurochem. *71*, 636–645. https://doi.org/10.1046/j.1471-4159.1998.71020636.x.
16. Semyanov, A., and Kullmann, D.M. (2000). Modulation of GABAergic signaling among interneurons by metabotropic glutamate receptors. Neuron *25*, 663–672. https://doi.org/10.1016/s0896-6273(00)81068-5.
17. Edwards, F.A., Konnerth, A., Sakmann, B., and Takahashi, T. (1989). A thin slice preparation for patch clamp recordings from neurones of the mammalian central nervous system. Pflugers Arch. *414*, 600–612. https://doi.org/10.1007/BF00580998.
18. Forsberg, M., Seth, H., Björefeldt, A., Lyckenvik, T., Andersson, M., Wasling, P., Zetterberg, H., and Hanse, E. (2019). Ionized calcium in human cerebrospinal fluid and its influence on intrinsic and synaptic excitability of hippocampal pyramidal neurons in the rat. J. Neurochem. *149*, 452–470. https://doi.org/10.1111/jnc.14693.
19. Dodge, F.A., Jr., and Rahamimoff, R. (1967). Co-operative action a calcium ions in transmitter release at the neuromuscular junction. J. Physiol. *193*, 419–432. https://doi.org/10.1113/jphysiol.1967.sp008367.
20. Tremblay, R., Lee, S., and Rudy, B. (2016). GABAergic Interneurons in the Neocortex: From Cellular Properties to Circuits. Neuron *91*, 260–292. https://doi.org/10.1016/j.neuron.2016.06.033.
21. Danbolt, N.C. (2001). Glutamate uptake. Prog. Neurobiol. *65*, 1–105. https://doi.org/10.1016/s0301-0082(00)00067-8.
22. Dickson, L., Teall, M., Chevalier, E., Cheung, T., Liwicki, G.M., Mack, S., Stephenson, A., White, K., Fosbeary, R., Harrison, D.C., et al. (2023). Discovery of CVN636: A Highly Potent, Selective, and CNS Penetrant mGluR(7) Allosteric Agonist. ACS Med. Chem. Lett. *14*, 442–449. https://doi.org/10.1021/acsmedchemlett.2c00529.
23. Herman, M.A., and Jahr, C.E. (2007). Extracellular glutamate concentration in hippocampal slice. J. Neurosci. *27*, 9736–9741. https://doi.org/10.1523/JNEUROSCI.3009-07.2007.
24. Scanziani, M., Salin, P.A., Vogt, K.E., Malenka, R.C., and Nicoll, R.A. (1997). Use-dependent increases in glutamate concentration activate presynaptic metabotropic glutamate receptors. Nature *385*, 630–634. https://doi.org/10.1038/385630a0.
25. von Gersdorff, H., Schneggenburger, R., Weis, S., and Neher, E. (1997). Presynaptic depression at a calyx synapse: the small contribution of metabotropic glutamate receptors. J. Neurosci. *17*, 8137–8146.
26. Schneggenburger, R., Meyer, A.C., and Neher, E. (1999). Released fraction and total size of a pool of immediately available transmitter quanta at a calyx synapse. Neuron *23*, 399–409. https://doi.org/10.1016/s0896-6273(00)80789-8.
27. Dittman, J.S., and Regehr, W.G. (1998). Calcium dependence and recovery kinetics of presynaptic depression at the climbing fiber to Purkinje cell synapse. J. Neurosci. *18*, 6147–6162.
28. Wang, L.Y., and Kaczmarek, L.K. (1998). High-frequency firing helps replenish the readily releasable pool of synaptic vesicles. Nature *394*, 384–388. https://doi.org/10.1038/28645.
29. Elmqvist, D., and Quastel, D.M. (1965). A quantitative study of end-plate potentials in isolated human muscle. J. Physiol. *178*, 505–529. https://doi.org/10.1113/jphysiol.1965.sp007639.
30. Ryan, T.A., Reuter, H., Wendland, B., Schweizer, F.E., Tsien, R.W., and Smith, S.J. (1993). The kinetics of synaptic vesicle recycling measured at single presynaptic boutons. Neuron *11*, 713–724. https://doi.org/10.1016/0896-6273(93)90081-2.

31. Stevens, C.F., and Tsujimoto, T. (1995). Estimates for the pool size of releasable quanta at a single central synapse and for the time required to refill the pool. Proc. Natl. Acad. Sci. USA *92*, 846–849. https://doi.org/10.1073/pnas.92.3.846.

32. Stevens, C.F., and Wesseling, J.F. (1998). Activity-dependent modulation of the rate at which synaptic vesicles become available to undergo exocytosis. Neuron *21*, 415–424. https://doi.org/10.1016/s0896-6273(00)80550-4.

33. Wang, Y., and Manis, P.B. (2008). Short-term synaptic depression and recovery at the mature mammalian endbulb of Held synapse in mice. J. Neurophysiol. *100*, 1255–1264. https://doi.org/10.1152/jn.90715.2008.

34. Wesseling, J.F., and Lo, D.C. (2002). Limit on the role of activity in controlling the release-ready supply of synaptic vesicles. J. Neurosci. *22*, 9708–9720.

35. Thanawala, M.S., and Regehr, W.G. (2016). Determining synaptic parameters using high-frequency activation. J. Neurosci. Methods *264*, 136–152. https://doi.org/10.1016/j.jneumeth.2016.02.021.

36. Ruiz, R., Cano, R., Casañas, J.J., Gaffield, M.A., Betz, W.J., and Tabares, L. (2011). Active zones and the readily releasable pool of synaptic vesicles at the neuromuscular junction of the mouse. J. Neurosci. *31*, 2000–2008.

37. Baldelli, P., Fassio, A., Valtorta, F., and Benfenati, F. (2007). Lack of synapsin I reduces the readily releasable pool of synaptic vesicles at central inhibitory synapses. J. Neurosci. *27*, 13520–13531. https://doi.org/10.1523/JNEUROSCI.3151-07.2007.

38. Bauman, A.L., Soughayer, J., Nguyen, B.T., Willoughby, D., Carnegie, G.K., Wong, W., Hoshi, N., Langeberg, L.K., Cooper, D.M.F., Dessauer, C.W., and Scott, J.D. (2006). Dynamic regulation of cAMP synthesis through anchored PKA-adenylyl cyclase V/VI complexes. Mol. Cell *23*, 925–931. https://doi.org/10.1016/j.molcel.2006.07.025.

39. Vaden, J.H., Banumurthy, G., Gusarevich, E.S., Overstreet-Wadiche, L., and Wadiche, J.I. (2019). The readily-releasable pool dynamically regulates multivesicular release. eLife *8*, e47434. https://doi.org/10.7554/eLife.47434.

40. Hosaka, M., Hammer, R.E., and Südhof, T.C. (1999). A phospho-switch controls the dynamic association of synapsins with synaptic vesicles. Neuron *24*, 377–387. https://doi.org/10.1016/S0896-6273(00)80851-X.

41. Hilfiker, S., Schweizer, F.E., Kao, H.T., Czernik, A.J., Greengard, P., and Augustine, G.J. (1998). Two sites of action for synapsin domain E in regulating neurotransmitter release. Nat. Neurosci. *1*, 29–35. https://doi.org/10.1038/229.

42. Greengard, P., Valtorta, F., Czernik, A.J., and Benfenati, F. (1993). Synaptic vesicle phosphoproteins and regulation of synaptic function. Science *259*, 780–785. https://doi.org/10.1126/science.8430330.

43. Rosahl, T.W., Spillane, D., Missler, M., Herz, J., Selig, D.K., Wolff, J.R., Hammer, R.E., Malenka, R.C., and Südhof, T.C. (1995). Essential functions of synapsins I and II in synaptic vesicle regulation. Nature *375*, 488–493. https://doi.org/10.1038/375488a0.

44. Esser, L., Wang, C.R., Hosaka, M., Smagula, C.S., Südhof, T.C., and Deisenhofer, J. (1998). Synapsin I is structurally similar to ATP-utilizing enzymes. EMBO J. *17*, 977–984. https://doi.org/10.1093/emboj/17.4.977.

45. Hilfiker, S., Benfenati, F., Doussau, F., Nairn, A.C., Czernik, A.J., Augustine, G.J., and Greengard, P. (2005). Structural domains involved in the regulation of transmitter release by synapsins. J. Neurosci. *25*, 2658–2669. https://doi.org/10.1523/JNEUROSCI.4278-04.2005.

46. Hosaka, M., and Südhof, T.C. (1998). Synapsins I and II are ATP-binding proteins with differential Ca2+ regulation. J. Biol. Chem. *273*, 1425–1429. https://doi.org/10.1074/jbc.273.3.1425.

47. Hosaka, M., and Südhof, T.C. (1998). Synapsin III, a novel synapsin with an unusual regulation by Ca2+. J. Biol. Chem. *273*, 13371–13374. https://doi.org/10.1074/jbc.273.22.13371.

48. Song, S.H., and Augustine, G.J. (2015). Synapsin Isoforms and Synaptic Vesicle Trafficking. Mol. Cells *38*, 936–940. https://doi.org/10.14348/molcells.2015.0233.

49. Kase, H., Iwahashi, K., Nakanishi, S., Matsuda, Y., Yamada, K., Takahashi, M., Murakata, C., Sato, A., and Kaneko, M. (1987). K-252 compounds, novel and potent inhibitors of protein kinase C and cyclic nucleotide-dependent protein kinases. Biochem. Biophys. Res. Commun. *142*, 436–440. https://doi.org/10.1016/0006-291x(87)90293-2.

50. Engh, R.A., Girod, A., Kinzel, V., Huber, R., and Bossemeyer, D. (1996). Crystal structures of catalytic subunit of cAMP-dependent protein kinase in complex with isoquinolinesulfonyl protein kinase inhibitors H7, H8, and H89. Structural implications for selectivity. J. Biol. Chem. *271*, 26157–26164. https://doi.org/10.1074/jbc.271.42.26157.

51. Murray, A.J. (2008). Pharmacological PKA inhibition: all may not be what it seems. Sci. Signal. *1*, re4. https://doi.org/10.1126/scisignal.122re4.

52. Jovanovic, J.N., Benfenati, F., Siow, Y.L., Sihra, T.S., Sanghera, J.S., Pelech, S.L., Greengard, P., and Czernik, A.J. (1996). Neurotrophins stimulate phosphorylation of synapsin I by MAP kinase and regulate synapsin I-actin interactions. Proc. Natl. Acad. Sci. USA *93*, 3679–3683. https://doi.org/10.1073/pnas.93.8.3679.

53. Jovanovic, J.N., Sihra, T.S., Nairn, A.C., Hemmings, H.C., Jr., Greengard, P., and Czernik, A.J. (2001). Opposing changes in phosphorylation of specific sites in synapsin I during Ca2+-dependent glutamate release in isolated nerve terminals. J. Neurosci. *21*, 7944–7953. https://doi.org/10.1523/JNEUROSCI.21-20-07944.2001.

54. Chi, P., Greengard, P., and Ryan, T.A. (2003). Synaptic vesicle mobilization is regulated by distinct synapsin I phosphorylation pathways at different frequencies. Neuron *38*, 69–78. https://doi.org/10.1016/s0896-6273(03)00151-x.

55. Perlini, L.E., Szczurkowska, J., Ballif, B.A., Piccini, A., Sacchetti, S., Giovedì, S., Benfenati, F., and Cancedda, L. (2015). Synapsin III acts downstream of semaphorin 3A/CDK5 signaling to regulate radial migration and orientation of pyramidal neurons in vivo. Cell Rep. *11*, 234–248. https://doi.org/10.1016/j.celrep.2015.03.022.

56. Piccini, A., Perlini, L.E., Cancedda, L., Benfenati, F., and Giovedì, S. (2015). Phosphorylation by PKA and Cdk5 Mediates the Early Effects of Synapsin III in Neuronal Morphological Maturation. J. Neurosci. *35*, 13148–13159. https://doi.org/10.1523/JNEUROSCI.1379-15.2015.

57. Verstegen, A.M.J., Tagliatti, E., Lignani, G., Marte, A., Stolero, T., Atias, M., Corradi, A., Valtorta, F., Gitler, D., Onofri, F., et al. (2014). Phosphorylation of synapsin I by cyclin-dependent kinase-5 sets the ratio between the resting and recycling pools of synaptic vesicles at hippocampal synapses. J. Neurosci. *34*, 7266–7280. https://doi.org/10.1523/JNEUROSCI.3973-13.2014.

58. Czernik, A.J., Pang, D.T., and Greengard, P. (1987). Amino acid sequences surrounding the cAMP-dependent and calcium/calmodulin-dependent phosphorylation sites in rat and bovine synapsin I. Proc. Natl. Acad. Sci. USA *84*, 7518–7522. https://doi.org/10.1073/pnas.84.21.7518.

59. Sun, J., Bronk, P., Liu, X., Han, W., and Südhof, T.C. (2006). Synapsins regulate use-dependent synaptic plasticity in the calyx of Held by a Ca2+/calmodulin-dependent pathway. Proc. Natl. Acad. Sci. USA *103*, 2880–2885. https://doi.org/10.1073/pnas.0511300103.

60. Keaveney, M.K., Rahsepar, B., Tseng, H.A., Fernandez, F.R., Mount, R.A., Ta, T., White, J.A., Berg, J., and Han, X. (2020). CaMKIIalpha-Positive Interneurons Identified via a microRNA-Based Viral Gene Targeting Strategy. J. Neurosci. *40*, 9576–9588. https://doi.org/10.1523/JNEUROSCI.2570-19.2020.

61. Veres, J.M., Andrasi, T., Nagy-Pal, P., and Hajos, N. (2023). CaMKIIalpha Promoter-Controlled Circuit Manipulations Target Both Pyramidal Cells

and Inhibitory Interneurons in Cortical Networks. eNeuro *10*. https://doi.org/10.1523/ENEURO.0070-23.2023.

62. Stewart, A.A., Ingebritsen, T.S., Manalan, A., Klee, C.B., and Cohen, P. (1982). Discovery of a Ca2+- and calmodulin-dependent protein phosphatase: probable identity with calcineurin (CaM-BP80). FEBS Lett. *137*, 80–84. https://doi.org/10.1016/0014-5793(82)80319-0.
63. Lazarevic, V., Fieńko, S., Andres-Alonso, M., Anni, D., Ivanova, D., Montenegro-Venegas, C., Gundelfinger, E.D., Cousin, M.A., and Fejtova, A. (2017). Physiological Concentrations of Amyloid Beta Regulate Recycling of Synaptic Vesicles via Alpha7 Acetylcholine Receptor and CDK5/Calcineurin Signaling. Front. Mol. Neurosci. *10*, 221. https://doi.org/10.3389/fnmol.2017.00221.
64. Rall, W. (2011). Core conductor theory and cable properties of neurons. Compr. Physiol. *1*, 39–97.
65. McCauley, J.P., Petroccione, M.A., D'Brant, L.Y., Todd, G.C., Affinnih, N., Wisnoski, J.J., Zahid, S., Shree, S., Sousa, A.A., De Guzman, R.M., et al. (2020). Circadian Modulation of Neurons and Astrocytes Controls Synaptic Plasticity in Hippocampal Area CA1. Cell Rep. *33*, 108255. https://doi.org/10.1016/j.celrep.2020.108255.
66. Williams, S.R., and Mitchell, S.J. (2008). Direct measurement of somatic voltage clamp errors in central neurons. Nat. Neurosci. *11*, 790–798. https://doi.org/10.1038/nn.2137.
67. Dodge, F.A., Jr., and Rahamimoff, R. (1967). On the relationship between calcium concentration and the amplitude of the end-plate potential. J. Physiol. *189*, 90P–92P.
68. Bezaire, M.J., and Soltesz, I. (2013). Quantitative assessment of CA1 local circuits: knowledge base for interneuron-pyramidal cell connectivity. Hippocampus *23*, 751–785. https://doi.org/10.1002/hipo.22141.
69. Bloss, E.B., Cembrowski, M.S., Karsh, B., Colonell, J., Fetter, R.D., and Spruston, N. (2016). Structured Dendritic Inhibition Supports Branch-Selective Integration in CA1 Pyramidal Cells. Neuron *89*, 1016–1030. https://doi.org/10.1016/j.neuron.2016.01.029.
70. Bittner, K.C., Grienberger, C., Vaidya, S.P., Milstein, A.D., Macklin, J.J., Suh, J., Tonegawa, S., and Magee, J.C. (2015). Conjunctive input processing drives feature selectivity in hippocampal CA1 neurons. Nat. Neurosci. *18*, 1133–1142. https://doi.org/10.1038/nn.4062.
71. Harvey, C.D., Collman, F., Dombeck, D.A., and Tank, D.W. (2009). Intracellular dynamics of hippocampal place cells during virtual navigation. Nature *461*, 941–946. https://doi.org/10.1038/nature08499.
72. Takahashi, H., and Magee, J.C. (2009). Pathway interactions and synaptic plasticity in the dendritic tuft regions of CA1 pyramidal neurons. Neuron *62*, 102–111. https://doi.org/10.1016/j.neuron.2009.03.007.
73. Larkum, M.E., Zhu, J.J., and Sakmann, B. (2001). Dendritic mechanisms underlying the coupling of the dendritic with the axonal action potential initiation zone of adult rat layer 5 pyramidal neurons. J. Physiol. *533*, 447–466. https://doi.org/10.1111/j.1469-7793.2001.0447a.x.
74. Hrabetová, S., and Nicholson, C. (2000). Dextran decreases extracellular tortuosity in thick-slice ischemia model. J. Cereb. Blood Flow Metab. *20*, 1306–1310. https://doi.org/10.1097/00004647-200009000-00005.
75. Savtchenko, L.P., and Rusakov, D.A. (2005). Extracellular diffusivity determines contribution of high-versus low-affinity receptors to neural signaling. Neuroimage *25*, 101–111. https://doi.org/10.1016/j.neuroimage.2004.11.020.
76. Scanziani, M., Gahwiler, B.H., and Thompson, S.M. (1995). Presynaptic inhibition of excitatory synaptic transmission by muscarinic and metabotropic glutamate receptor activation in the hippocampus: are Ca2+ channels involved? Neuropharmacology *34*, 1549–1557. https://doi.org/10.1016/0028-3908(95)00119-q.
77. Stemmer, P.M., and Klee, C.B. (1994). Dual calcium ion regulation of calcineurin by calmodulin and calcineurin B. Biochemistry *33*, 6859–6866. https://doi.org/10.1021/bi00188a015.
78. Gitler, D., Takagishi, Y., Feng, J., Ren, Y., Rodriguiz, R.M., Wetsel, W.C., Greengard, P., and Augustine, G.J. (2004). Different presynaptic roles of synapsins at excitatory and inhibitory synapses. J. Neurosci. *24*, 11368–11380. https://doi.org/10.1523/JNEUROSCI.3795-04.2004.
79. Matthews, E.A., and Dietrich, D. (2015). Buffer mobility and the regulation of neuronal calcium domains. Front. Cell. Neurosci. *9*, 48. https://doi.org/10.3389/fncel.2015.00048.
80. Rusakov, D.A., and Kullmann, D.M. (1998). Extrasynaptic glutamate diffusion in the hippocampus: ultrastructural constraints, uptake, and receptor activation. J. Neurosci. *18*, 3158–3170. https://doi.org/10.1523/JNEUROSCI.18-09-03158.1998.
81. Merchán-Pérez, A., Rodriguez, J.R., Ribak, C.E., and DeFelipe, J. (2009). Proximity of excitatory and inhibitory axon terminals adjacent to pyramidal cell bodies provides a putative basis for nonsynaptic interactions. Proc. Natl. Acad. Sci. USA *106*, 9878–9883. https://doi.org/10.1073/pnas.0900330106.
82. Peukes, J., Lovatt, C., Leistner, C., Boulanger, J., Morado, D.R., Fuller, M.J.G., Kukulski, W., Zhu, F., Komiyama, N.H., Briggs, J.A.G., et al. (2025). The molecular infrastructure of glutamatergic synapses in the mammalian forebrain. eLife *13*. https://doi.org/10.7554/eLife.100335.
83. Tao, H.W., and Poo, M. (2001). Retrograde signaling at central synapses. Proc. Natl. Acad. Sci. USA *98*, 11009–11015. https://doi.org/10.1073/pnas.191351698.
84. Regehr, W.G., Carey, M.R., and Best, A.R. (2009). Activity-dependent regulation of synapses by retrograde messengers. Neuron *63*, 154–170. https://doi.org/10.1016/j.neuron.2009.06.021.
85. Dietrich, D., Kral, T., Clusmann, H., Friedl, M., and Schramm, J. (1999). Reduced function of L-AP4-sensitive metabotropic glutamate receptors in human epileptic sclerotic hippocampus. Eur. J. Neurosci. *11*, 1109–1113. https://doi.org/10.1046/j.1460-9568.1999.00549.x.
86. Bough, K.J., Mott, D.D., and Dingledine, R.J. (2004). Medial perforant path inhibition mediated by mGluR7 is reduced after status epilepticus. J. Neurophysiol. *92*, 1549–1557. https://doi.org/10.1152/jn.00315.2004.
87. Kral, T., Erdmann, E., Sochivko, D., Clusmann, H., Schramm, J., and Dietrich, D. (2003). Down-regulation of mGluR8 in pilocarpine epileptic rats. Synapse *47*, 278–284. https://doi.org/10.1002/syn.10178.
88. Garrido-Sanabria, E.R., Otalora, L.F.P., Arshadmansab, M.F., Herrera, B., Francisco, S., and Ermolinsky, B.S. (2008). Impaired expression and function of group II metabotropic glutamate receptors in pilocarpine-treated chronically epileptic rats. Brain Res. *1240*, 165–176. https://doi.org/10.1016/j.brainres.2008.08.084.
89. Pacheco Otalora, L.F., Couoh, J., Shigamoto, R., Zarei, M.M., and Garrido Sanabria, E.R. (2006). Abnormal mGluR2/3 expression in the perforant path termination zones and mossy fibers of chronically epileptic rats. Brain Res. *1098*, 170–185. https://doi.org/10.1016/j.brainres.2006.04.124.
90. Ghauri, M., Chapman, A.G., and Meldrum, B.S. (1996). Convulsant and anticonvulsant actions of agonists and antagonists of group III mGluRs. Neuroreport *7*, 1469–1474. https://doi.org/10.1097/00001756-199606170-00005.
91. Abdul-Ghani, A.S., Attwell, P.J., Singh Kent, N., Bradford, H.F., Croucher, M.J., and Jane, D.E. (1997). Anti-epileptogenic and anticonvulsant activity of L-2-amino-4-phosphonobutyrate, a presynaptic glutamate receptor agonist. Brain Res. *755*, 202–212. https://doi.org/10.1016/s0006-8993(97)00098-x.
92. Chapman, A.G., Nanan, K., Yip, P., and Meldrum, B.S. (1999). Anticonvulsant activity of a metabotropic glutamate receptor 8 preferential agonist, (R,S)-4-phosphonophenylglycine. Eur. J. Pharmacol. *383*, 23–27. https://doi.org/10.1016/s0014-2999(99)00615-9.
93. Chapman, A.G., Talebi, A., Yip, P.K., and Meldrum, B.S. (2001). Anticonvulsant activity of a mGlu(4alpha) receptor selective agonist, (1S,3R,4S)-1-aminocyclopentane-1,2,4-tricarboxylic acid. Eur. J. Pharmacol. *424*, 107–113. https://doi.org/10.1016/s0014-2999(01)01013-5.
94. Folbergrová, J., Haugvicová, R., and Mares, P. (2003). Seizures induced by homocysteic acid in immature rats are prevented by group III metabotropic

glutamate receptoragonist (R,S)-4-phosphonophenylglycine. Exp. Neurol. *180*, 46–54. https://doi.org/10.1016/s0014-4886(02)00047-x.

95. Moldrich, R.X., Jeffrey, M., Talebi, A., Beart, P.M., Chapman, A.G., and Meldrum, B.S. (2001). Anti-epileptic activity of group II metabotropic glutamate receptor agonists (–)-2-oxa-4-aminobicyclo[3.1.0]hexane-4,6-dicarboxylate (LY379268) and (–)-2-thia-4-aminobicyclo[3.1.0]hexane-4,6-dicarboxylate (LY389795). Neuropharmacology *41*, 8–18. https://doi.org/10.1016/s0028-3908(01)00044-2.

96. Sansig, G., Bushell, T.J., Clarke, V.R., Rozov, A., Burnashev, N., Portet, C., Gasparini, F., Schmutz, M., Klebs, K., Shigemoto, R., et al. (2001). Increased seizure susceptibility in mice lacking metabotropic glutamate receptor 7. J. Neurosci. *21*, 8734–8745. https://doi.org/10.1523/JNEUROSCI.21-22-08734.2001.

97. Gasparini, F., Bruno, V., Battaglia, G., Lukic, S., Leonhardt, T., Inderbitzin, W., Laurie, D., Sommer, B., Varney, M.A., Hess, S.D., et al. (1999). (R,S)-4-phosphonophenylglycine, a potent and selective group III metabotropic glutamate receptor agonist, is anticonvulsive and neuroprotective in vivo. J. Pharmacol. Exp. Ther. *289*, 1678–1687.

98. Mares, P., and Mikulecká, A. (2004). MPEP, an antagonist of metabotropic glutamate receptors, exhibits anticonvulsant action in immature rats without a serious impairment of motor performance. Epilepsy Res. *60*, 17–26. https://doi.org/10.1016/j.eplepsyres.2004.04.008.

99. Tizzano, J.P., Griffey, K.I., and Schoepp, D.D. (1995). Receptor subtypes linked to metabotropic glutamate receptor agonist-mediated limbic seizures in mice. Ann. N. Y. Acad. Sci. *765*, 230–248. https://doi.org/10.1111/j.1749-6632.1995.tb16579.x.

100. Tang, E., Yip, P.K., Chapman, A.G., Jane, D.E., and Meldrum, B.S. (1997). Prolonged anticonvulsant action of glutamate metabotropic receptor agonists in inferior colliculus of genetically epilepsy-prone rats. Eur. J. Pharmacol. *327*, 109–115. https://doi.org/10.1016/s0014-2999(97)89649-5.

101. Grienberger, C., Milstein, A.D., Bittner, K.C., Romani, S., and Magee, J.C. (2017). Inhibitory suppression of heterogeneously tuned excitation enhances spatial coding in CA1 place cells. Nat. Neurosci. *20*, 417–426. https://doi.org/10.1038/nn.4486.

102. Geiller, T., Vancura, B., Terada, S., Troullinou, E., Chavlis, S., Tsagkatakis, G., Tsakalides, P., Ócsai, K., Poirazi, P., Rózsa, B.J., and Losonczy, A. (2020). Large-Scale 3D Two-Photon Imaging of Molecularly Identified CA1 Interneuron Dynamics in Behaving Mice. Neuron *108*, 968–983.e9. https://doi.org/10.1016/j.neuron.2020.09.013.

103. Valero, M., Navas-Olive, A., de la Prida, L.M., and Buzsáki, G. (2022). Inhibitory conductance controls place field dynamics in the hippocampus. Cell Rep. *40*, 111232. https://doi.org/10.1016/j.celrep.2022.111232.

104. Mau, W., Hasselmo, M.E., and Cai, D.J. (2020). The brain in motion: How ensemble fluidity drives memory-updating and flexibility. eLife *9*, e63550. https://doi.org/10.7554/eLife.63550.

105. Bittner, K.C., Milstein, A.D., Grienberger, C., Romani, S., and Magee, J.C. (2017). Behavioral time scale synaptic plasticity underlies CA1 place fields. Science *357*, 1033–1036. https://doi.org/10.1126/science.aan3846.

106. Quraishi, S., Gayet, J., Morgans, C.W., and Duvoisin, R.M. (2007). Distribution of group-III metabotropic glutamate receptors in the retina. J. Comp. Neurol. *501*, 931–943. https://doi.org/10.1002/cne.21274.

107. Tomioka, N.H., Yasuda, H., Miyamoto, H., Hatayama, M., Morimura, N., Matsumoto, Y., Suzuki, T., Odagawa, M., Odaka, Y.S., Iwayama, Y., et al. (2014). Elfn1 recruits presynaptic mGluR7 in trans and its loss results in seizures. Nat. Commun. *5*, 4501. https://doi.org/10.1038/ncomms5501.

108. Kinoshita, A., Ohishi, H., Nomura, S., Shigemoto, R., Nakanishi, S., and Mizuno, N. (1996). Presynaptic localization of a metabotropic glutamate receptor, mGluR4a, in the cerebellar cortex: a light and electron microscope study in the rat. Neurosci. Lett. *207*, 199–202. https://doi.org/10.1016/0304-3940(96)12519-2.

109. Beattie, R., Postiglione, M.P., Burnett, L.E., Laukoter, S., Streicher, C., Pauler, F.M., Xiao, G., Klezovitch, O., Vasioukhin, V., Ghashghaei, T.H., and Hippenmeyer, S. (2017). Mosaic Analysis with Double Markers Reveals Distinct Sequential Functions of Lgl1 in Neural Stem Cells. Neuron *94*, 517–533.e3. https://doi.org/10.1016/j.neuron.2017.04.012.

110. Kinoshita, A., Ohishi, H., Neki, A., Nomura, S., Shigemoto, R., Takada, M., Nakanishi, S., and Mizuno, N. (1996). Presynaptic localization of a metabotropic glutamate receptor, mGluR8, in the rhinencephalic areas: a light and electron microscope study in the rat. Neurosci. Lett. *207*, 61–64. https://doi.org/10.1016/0304-3940(96)12489-7.

111. Melone, M., Ciriachi, C., Pietrobon, D., and Conti, F. (2019). Heterogeneity of Astrocytic and Neuronal GLT-1 at Cortical Excitatory Synapses, as Revealed by its Colocalization With Na+/K+-ATPase alpha Isoforms. Cereb. Cortex *29*, 3331–3350. https://doi.org/10.1093/cercor/bhy203.

112. Aoki, C. (1992). Beta-Adrenergic Receptors - Astrocytic Localization in the Adult Visual-Cortex and Their Relation to Catecholamine Axon Terminals as Revealed by Electron-Microscopic Immunocytochemistry. J. Neurosci. *12*, 781–792.

113. Yi, H., Leunissen, J., Shi, G., Gutekunst, C., and Hersch, S. (2001). A novel procedure for pre-embedding double immunogold-silver labeling at the ultrastructural level. J. Histochem. Cytochem. *49*, 279–284. https://doi.org/10.1177/002215540104900301.

114. Li, S., Liu, N., Yao, L., Zhang, X., Zhou, D., and Cai, D. (2019). Determination of effective synaptic conductances using somatic voltage clamp. PLoS Comput. Biol. *15*, e1006871. https://doi.org/10.1371/journal.pcbi.1006871.

115. Cobb, E.A.W., Petroccione, M.A., and Scimemi, A. (2023). NRN-EZ: an application to streamline biophysical modeling of synaptic integration using NEURON. Sci. Rep. *13*, 464. https://doi.org/10.1038/s41598-022-27302-8.

116. Spruston, N., Jaffe, D.B., Williams, S.H., and Johnston, D. (1993). Voltage- and space-clamp errors associated with the measurement of electrotonically remote synaptic events. J. Neurophysiol. *70*, 781–802. https://doi.org/10.1152/jn.1993.70.2.781.

117. Soltesz, I., Smetters, D.K., and Mody, I. (1995). Tonic inhibition originates from synapses close to the soma. Neuron *14*, 1273–1283. https://doi.org/10.1016/0896-6273(95)90274-0.

118. Peters, A. (1991). The fine structure of the nervous system. In Neurons and Their Supporting Cells (Oxford University Press), pp. 211–218.

119. DeFelipe, J., Marco, P., Busturia, I., and Merchán-Pérez, A. (1999). Estimation of the number of synapses in the cerebral cortex: methodological considerations. Cereb. Cortex *9*, 722–732. https://doi.org/10.1093/cercor/9.7.722.

120. DeFelipe, J. (2002). Cortical interneurons: from Cajal to 2001. Prog. Brain Res. *136*, 215–238. https://doi.org/10.1016/s0079-6123(02)36019-9.

121. Mariotti, L., Losi, G., Lia, A., Melone, M., Chiavegato, A., Gómez-Gonzalo, M., Sessolo, M., Bovetti, S., Forli, A., Zonta, M., et al. (2018). Interneuron-specific signaling evokes distinctive somatostatin-mediated responses in adult cortical astrocytes. Nat. Commun. *9*, 82. https://doi.org/10.1038/s41467-017-02642-6.

122. Petilla Interneuron Nomenclature Group; Ascoli, G.A., Alonso-Nanclares, L., Anderson, S.A., Barrionuevo, G., Benavides-Piccione, R., Burkhalter, A., Buzsáki, G., Cauli, B., Defelipe, J., et al. (2008). Petilla terminology: nomenclature of features of GABAergic interneurons of the cerebral cortex. Nat. Rev. Neurosci. *9*, 557–568. https://doi.org/10.1038/nrn2402.

123. Melone, M., Ciappelloni, S., and Conti, F. (2014). Plasma membrane transporters GAT-1 and GAT-3 contribute to heterogeneity of

GABAergic synapses in neocortex. Front. Neuroanat. *8*, 72. https://doi.org/10.3389/fnana.2014.00072.

124. Somogyi, P., Tamás, G., Lujan, R., and Buhl, E.H. (1998). Salient features of synaptic organisation in the cerebral cortex. Brain Res. Brain Res. Rev. *26*, 113–135. https://doi.org/10.1016/s0165-0173(97)00061-1.

125. Skaggs, W., Mcnaughton, B., and Gothard, K. (1992). An information-theoretic approach to deciphering the hippocampal code. Adv. Neural Inf. Process. Syst. *5*.

126. Treves, A., and Rolls, E.T. (1991). What determines the capacity of autoassociative memories in the brain? Network *2*, 371–397.

STAR★METHODS

KEY RESOURCES TABLE

REAGENT or RESOURCE	SOURCE	IDENTIFIER
Antibodies		
Rabbit anti-mGluR4a	F. Ferraguti	RRID: AB_23147894
Rabbit anti-mGluR7a	Millipore Sigma	RRID: AB_310459
Guinea pig anti-mGluR4a	F. Ferraguti	RRID: AB_2314798
Goat anti-tdTomato	OriGene	RRID: AB_2722750
Donkey anti-rabbit	Jackson Immunoresearch	RRID: AB_2340594
Donkey anti-guinea pig	Jackson Immunoresearch	RRID: AB_2340452
Donkey anti-goat	AURION	RRID: AB_2943420
Bacterial and virus strains		
AAV5-EF1a-DIO-hChR2(H134R)-EYFP-WPRE-pA	UNC	N/A
Chemicals, peptides, and recombinant proteins		
D,L-2-Amino-5phosphonopentanoic acid	HelloBio	N/A
2,3-Dioxo6-nitro-1,2,3,4-tetrahydrobenzo[f] quinoxaline-7-sulfonamide disodium salt	HelloBio	N/A
MMPIP	Abcam	N/A
MSOP	Abcam	N/A
Sulforhodamine 101	Millipore Sigma	N/A
Tetrodotoxin	HelloBio	N/A
Texas Red dextran 10 KDa	ThermoFisher Scientific	N/A
(3S)-3-[[3-[[4-(Trifluoromethyl)benzoyl]amino]phenyl] methoxy]-L-aspartic acid	Tocris	N/A
Critical commercial assays		
KAPA HiFi Hot Start Ready Mix PCR Kit	KAPA Biosystems	N/A
Deposited data		
Open Science Framework repository	https://osf.io/ucj2d/	N/A
NEURON simulations	https://modeldb.science/2031084	N/A
Github repository	https://github.com/scimemia/mGluRIII	N/A
Zenodo repository	https://doi.org/10.5281/zenodo.19455971	N/A
Experimental models: Organisms/strains		
C57BL/6J	Jackson Lab	RRID:IMSR_JAX:000664
B6.129P2-Pvalb$^{tm1(cre)Arbr}$/J	Jackson Lab	RRID:IMSR_JAX:017320
B6N.Cg-Sst$^{tm2.1(cre)Zjh}$/J	Jackson Lab	RRID:IMSR_JAX:018973
B6.Cg-Gt(ROSA)26Sor$^{tm9(CAG-tdTomato)Hze}$/J	Jackson Lab	RRID:IMSR_JAX:007909
B6;129-Syn2^{tm1Pggd} Syn3^{tm1Pggd} Syn1^{tm1Pggd}/Mmjax	MMRRC	RRID:MMRRC_041434-JAX
Oligonucleotides		
AAG GGA GCT GCA GTG GAG TA	Eurofins Genomics	N/A
CCG AAA ATC TGT GGG AAG TC	Eurofins Genomics	N/A
CTG TTC CTG TAC GGC ATG G	Eurofins Genomics	N/A
GGC ATT AAA GCA GCG TAT CC	Eurofins Genomics	N/A
CAG AGC AGG CAT GGT GAC TA	Eurofins Genomics	N/A
AGT ACC AAG CAG GCA GGA GA	Eurofins Genomics	N/A
AAA TGC TTC TGT CCG TTT GC	Eurofins Genomics	N/A
ATG TTT AGC TGG CCC AAA TG	Eurofins Genomics	N/A
GAG GTC TGC CAA CTC GAA C	Eurofins Genomics	N/A

(*Continued on next page*)

Continued

REAGENT or RESOURCE	SOURCE	IDENTIFIER
AGT CAA ACG CTT GCT CTT CA	Eurofins Genomics	N/A
TCA GGT ACA TGG ATC CAC TAG TTC T	Eurofins Genomics	N/A
AGG GAG TTT CGT TAC TAC AGG TCC	Eurofins Genomics	N/A
AGA TTG GCC ATG AAG TTG CTG TCC	Eurofins Genomics	N/A
CTA CTT CCA TTT GTC ACG TCC TGC	Eurofins Genomics	N/A
CTC CTC TTG AAA CCA CGA AG	Eurofins Genomics	N/A
TAC TTC TGT CTC CGC CCC TCT	Eurofins Genomics	N/A
AGA CTG CCT TGG GAA AAG CG	Eurofins Genomics	N/A
GAA CCT GTG CGA AAC AGT TG	Eurofins Genomics	N/A
GTG TGG GGG TTC ATA CCT GT	Eurofins Genomics	N/A
CTC GAC ATT GGG TGG AAA CA	Eurofins Genomics	N/A

EXPERIMENTAL MODEL AND STUDY PARTICIPANT DETAILS

Mice

All experimental procedures were performed in accordance with the guidelines of the National Institutes of Health and were approved by the Institutional Animal Care and Use Committee at the State University of New York (SUNY) Albany (Protocol 24-002 approved on 02/27/2024), Brandeis University (Protocol 25001, approved on 08/06/2024) and guidelines described in the National Institutes of Health's Guide for the Care and Use of Laboratory Animals. The number of mice used for the experiments described in this work are consistent with the number of mice approved by approved IACUC protocols. Unless otherwise stated, all mice were group housed and kept under 12 h:12 h light:dark conditions. Food and water were available *ad libitum* to all mice throughout the 24-h period. For our experiments, we used mice of either sex from the mouse lines reported below. *In vitro* electrophysiology experiments were performed in 4–8 week old mice. *In vivo* electrophysiology experiments were performed in 8–14 week old mice.

Mouse line	RRID	Referred to as
C57BL/6NJ	RRID:IMSR_JAX:000664	WT
B6.129P2-Pvalb$^{tm1(cre)Arbr}$/J	RRID:IMSR_JAX:017320	PV$^{Cre/+}$
B6N.Cg-Sst$^{tm2.1(cre)Zjh}$/J	RRID:IMSR_JAX:018973	SST$^{Cre/+}$
B6.Cg-Gt(ROSA)26Sor$^{tm9(CAG-tdTomato)Hze}$/J	RRID:IMSR_JAX:007909	Ai9$^{Tg/Tg}$
B6;129-Syn2^{tm1Pggd} Syn3^{tm1Pggd} Syn1^{tm1Pggd}/Mmjax	RRID:MMRRC_041434-JAX	Syn TKO

Genotyping was performed on toe tissue samples of P7–P10 mice. Briefly, tissue samples were digested at 55°C overnight with shaking at 330 rpm in a lysis buffer containing the following (in mM): 100 Tris-HCl base, pH 8, 5 EDTA, and 200 NaCl, along with 0.2% SDS and 100 mg/mL proteinase K. Following heat inactivation of Proteinase K at 97°C for 10 min, DNA samples were diluted 1:1 with nuclease-free water. The PCR primers were purchased from Eurofins Genomics and their nucleotide sequences are listed below.

Gene	Forward primer	Reverse primer	Band size (bp)
Ai9	WT 5′ AAG GGA GCT GCA GTG GAG TA 3′ Mut 5′ CTG TTC CTG TAC GGC ATG G 3′	WT 5′ CCG AAA ATC TGT GGG AAG TC 3′ Mut 5′ GGC ATT AAA GCA GCG TAT CC 3′	297 196
Pvalb	WT 5′ CAG AGC AGG CAT GGT GAC TA 3′ Mut 5′ AAA TGC TTC TGT CCG TTT GC 3′	WT 5′ AGT ACC AAG CAG GCA GGA GA 3′ Mut 5′ ATG TTT AGC TGG CCC AAA TG 3′	500 163
Sst	WT 5′ GAG GTC TGC CAA CTC GAA C 3′ Mut 5′ TCA GGT ACA TGG ATC CAC TAG TTC T 3′	WT 5′ AGT CAA ACG CTT GCT CTT CA 3′	257 198
Syn1	WT 5′ AGG GAG TTT CGT TAC TAC AGG TCC 3′	WT 5′AGA TTG GCC ATG AAG TTG CTG TCC 3′ Mut 5′ CTA CTT CCA TTT GTC ACG TCC TGC 3′	543 750
Syn2	WT 5′ CTC CTC TTG AAA CCA CGA AG 3′	WT 5′ TAC TTC TGT CTC CGC CCC TCT 3′ Mut 5′ AGA CTG CCT TGG GAA AAG CG 3′	211 135
Syn3	WT 5′ GAA CCT GTG CGA AAC AGT TG 3′ Mut 5′ CTC GAC ATT GGG TGG AAA CA 3′	WT 5′ GTG TGG GGG TTC ATA CCT GT 3′	367 200

PCR was carried out using the KAPA HiFi Hot Start Ready Mix PCR Kit (KAPA Biosystems, KK2602). Briefly, 12.5 μL of 2× KAPA HiFi Hot Start Ready Mix was added to 11.5 μL of a diluted primer mix (0.5–0.75 mM final concentration for each primer) and 1 μL of diluted DNA. The PCR cycling protocols are described in the table below.

Ai9, Pvalb, Sst, Syn2	Initiation/melting	Denaturation	Annealing	Elongation	Amplification	Hold
Temperature (°C)	95	95	60	72	72	4
Duration (min)	3	0.25	0.25	0.25	1	∞
Cycles	1	35			1	
Syn1	**Initiation/melting**	**Denaturation**	**Annealing**	**Elongation**	**Amplification**	**Hold**
Temperature (°C)	95	95	56	72	72	4
Duration (min)	3	0.25	0.25	0.5	1	∞
Cycles	1	35			1	
Syn3	**Initiation/melting**	**Denaturation**	**Annealing**	**Elongation**	**Amplification**	**Hold**
Temperature (°C)	95	95	64	72	72	4
Duration (min)	3	0.25	0.25	0.25	1	∞
Cycles	1	35			1	

METHOD DETAILS

Stereotaxic intracranial AAV injections

AAV5-EF1a-DIO-hChR2(H134R)-EYFP-WPRE-pA (University of North Carolina Vector Core, Chapel Hill, NC) was injected into $PV^{Cre/+}$ and $SST^{Cre/+}$ mice. Male and female mice (P14-16) were anesthetized with isoflurane (induction: 5% in 100% O_2 at 1–2 L/min; maintenance: 3% in 100% O_2 at 1–2 L/min) and placed in the stereotaxic frame of a motorized drill and injection robot (Neurostar GmbH, Tübingen, Germany). After making a skin incision and thinning the skull under aseptic conditions, we injected 200 nL of the viral constructs bilaterally in *stratum radiatum* using a Hamilton syringe at a rate of 50 nL/min. The injection coordinates from bregma were AP: −1.9 mm, ML: ±1.6 mm, DV: −1.4 mm. After the stereotaxic injections, the mice were returned to their home cage and used for slice physiology experiments 2–6 weeks after surgery.

Acute slice preparation

Acute coronal slices of the mouse hippocampus were obtained from C57BL/6J mice of either sex (4–8 week old), deeply anesthetized with isoflurane and decapitated in accordance with SUNY Albany Animal Care and Use Committee guidelines. The brain was rapidly removed and placed in ice-cold slicing solution bubbled with 95%O_2/5%CO_2 containing the following (in mM): 119 NaCl, 2.5 KCl, 0.5 $CaCl_2$, 1.3 $MgSO_4{\cdot}H_2O$, 4 $MgCl_2$, 26.2 $NaHCO_3$, 1 NaH_2PO_4, and 22 glucose, 320 mOsm, pH 7.4. The slices (250 μm thick) were prepared using a vibrating blade microtome (VT1200S; Leica Microsystems, Buffalo Grove, IL). Once prepared, the slices were stored in slicing solution in a submersion chamber at 36°C for 30 min and at RT for at least 30 min and up to 5 h.

In vitro electrophysiology recordings and optogenetics

Unless otherwise stated, the recording solution contained the following (in mM): 119 NaCl, 2.5 KCl, 1.2 $CaCl_2$, 1 $MgCl_2$, 26.2 $NaHCO_3$, and 1 NaH_2PO_4, 22 glucose, 300 mOsm, pH 7.4. We identified the hippocampus under bright field illumination using an upright fixed-stage microscope (BX51 WI; Evident, Waltham, MA). To record electrically evoked currents, we delivered constant voltage stimuli (50–100 ms) to a bipolar stainless-steel electrode (Cat# MX21AES(JD3); Frederick Haer Corporation, Bowdoin, ME) positioned in *stratum radiatum*, ∼100 μm away from the recorded cell. To activate ChR2-expressing fibers from PV- and SST-INs, we used 5 ms-long light pulses generated by a SOLA-SE light engine (Lumencor, Beaverton, OR) and filtered using a green FITC filter set (469/497/525 nm). The light power at the sample plane was ∼250 μW and the light pulses were delivered at intervals of 30 s using whole-field illumination through a 40× water immersion objective (LUMPLFLN40XW; Evident, Waltham, MA). When testing the effect of PKA inhibition, we incubated the hippocampal slices with KT5720 (1 μM) for 30–60 min prior to recording. Whole-cell, voltage-clamp patch-clamp recordings were made using patch pipettes containing (in mM): 120 $CsCH_3SO_3$, 10 EGTA, 20 HEPES, 2 MgATP, 0.2 NaGTP, 5 QX-314Br, 290 mOsm, pH 7.2. IPSCs were recorded at a holding potential of 0 mV (the reversal potential for glutamatergic currents), in the presence of the AMPA receptor antagonist 2,3-Dioxo-6-nitro-1,2,3,4-tetrahydrobenzo[f]quinoxaline-7-sulfonamide disodium salt (NBQX, 10 μM) and the NMDA receptor antagonist D,L-2-Amino-5-phosphonopentanoic acid (APV, 50 μM). EPSCs were recorded at a holding potential of −70 mV (the reversal potential for GABAergic currents), in the presence of the $GABA_A$ receptor antagonist picrotoxin (100 μM). For RuBi-GABA uncaging experiments, slices were perfused with RuBi-GABA (5 μM), NBQX (10 μM) and APV (50 μM), and uIPSCs were recorded at a holding potential of 0 mV. RuBi-GABA was uncaged using

light flashed (5 ms, delivered every 30 s) generated by a SOLA-SE light engine (Lumencor, Beaverton, OR) connected to the epi-illumination port. The output of the light engine was passed through a FITC filter set (469/497/525 nm) and was set to fill the entire back aperture of the (Evident LUMPLFLN 40XW). Consequently, the entire field of view was illuminated with a collimated beam, corresponding to an uncaging area of ~662.5 μm diameter (i.e., field number/magnification of the objective: 26.5/40). The light power at the ample plane was ~250 μW. All recordings were obtained using a Multiclamp 700B amplifier (Molecular Devices, San Jose, CA) and filtered at 10 KHz, converted with an 18-bit 200 kHz A/D board (HEKA Instrument, Holliston, MA), digitized at 10 KHz, and analyzed offline with custom-made software (A. S.) written in IgorPro 6.37 (Wavemetrics, Lake Oswego, OR). Patch electrodes (#0010 glass; Harvard Apparatus, Holliston, MA) had tip resistances of ~5 MΩ. Series resistance (~20 MΩ) was not compensated but was continuously monitored and experiments were discarded if this changed by >20%. The series resistance was subtracted from the total resistance to estimate the cell membrane resistance of neurons and astrocytes. Extracellular recordings were performed using electrodes with a tip resistance of 2-5MΩ, filled with the recording solution described above. The electrode resistance was continuously monitored, and experiments were discarded if this changed by >20%. Tetrodotoxin (TTX), NBQX and APV were purchased from Hello Bio (Princeton, NJ; Cat# HB1035, HB0443, HB0251, respectively). (3S)-3-[[3-[[4-(Trifluoromethyl)benzoyl]amino]-phenyl]methoxy]-L-aspartic acid (T-TBOA) was purchased from Tocris (Minneapolis, MN; Cat# 2532). MSOP and MMPIP were purchased from Abcam (Waltham, MA; Cat# ab141381 and ab120245, respectively). All other chemicals were purchased from Millipore Sigma (Burlington, MA). All recordings were performed at RT.

Surgeries for *in vivo* electrophysiology experiments and training

All mice were housed under a reversed 12-h light/12-h dark cycle. All surgical procedures were performed under deep isoflurane anesthesia (4% induction, 2–3% maintenance). After locally applying topical anesthetics, the scalp was removed and cleaned. Then the skull was leveled, and locations for the craniotomies for the whole-cell patch clamp and LFP recordings were marked using stereotactic coordinates (whole-cell recordings: AP -2.0 mm, ML ±1.7 mm; LFP recordings: AP -3.55 mm, ML ±1.7 mm). Then, the skull was covered with cyanoacrylate glue (Loctite). As soon as the glue had dried, custom-made titanium head bars with an opening over the hippocampus were attached to the skull using dental acrylic (Ortho-Jet, Lang Dental). Following at least a week of recovery, mice were placed on water restriction (1.5 mL/day). After at least 3 days of water restriction mice were handled by the experimenter for at least five days (15 min/day). Next, mice were trained to run on the treadmill for a 10% sucrose (in water) reward delivered through a licking port once for every complete rotation of the belt, i.e., a lap of 200 cm. Mice were supplemented with additional water after training sessions to guarantee a daily water intake of 1.5 mL/day. Mice were trained until the number of laps completed per day was >100 laps/hr and was comparable for 2–3 days. The typical treadmill training duration was 4–7 days. The day before the first recording session, two small craniotomies (∅ = 0.5 mm), one for the whole-cell patch and one for the LFP electrode, were drilled at the previously marked positions under isoflurane anesthesia. The dura was, if possible, left intact, and the craniotomies were covered with a biocompatible silicone elastomer (KWICK-CAST, World Precision Instrument, Sarasota, FL).

Behavioral setup

The linear track treadmill consisted of a belt made from velvet fabric (McMaster Carr) enriched with visual and tactile cues.[70,101,105] The belt was self-propelled and divided up into three sectors, each with a different type of local cue. The sucrose/water reward (5–7 μL) was delivered through a custom-made lick port controlled by a solenoid valve (Lee Company, Westbrook, CT), at a point located 130 cm from the beginning of the belt. A single photoelectric sensor (Sparkfun, Niwot, CO) was used to reset the location measurement in each lap (=lap start). The mouse running speed was measured using an encoder attached to one of the wheel axles (Cat# HEDS–5540#I06, Avago, San Jose, CA). The valve, sensor, and encoder were controlled with microprocessor-controlled behavioral control system (Bpod, Sanworks, Rochester, NY). A separate Arduino Teensy 3.5 microprocessor interfaced with a custom-made MATLAB GUI was used to control the current injections based on the position of the mouse on the belt.

In vivo electrophysiology

All whole-cell recordings were made in current clamp mode using a model 2400 patch-clamp amplifier (A-M Systems, Sequim, WA). The LFP recordings were conducted using either the model 2400 patch-clamp amplifier or a model 1700 differential AC amplifier (A-M Systems, Sequim, WA). All signals were digitized at 20 kHz using the National Instruments PCIe-6341 card and the open-access MATLAB-based software (WaveSurfer, Janelia Research Campus). Liquid junction potentials were not corrected. CA1-PC recordings were either aborted or excluded from further analysis if access resistance exceeded a predefined threshold of 50 MΩ. For each mouse, the first step involved determining the depth of the CA1-PC layer using the LFP signals. Glass electrodes (1.5–3.5 MΩ), filled with 0.9% NaCl, were mounted vertically on the micromanipulator to be used later for the whole-cell recordings (Luigs and Neumann, Ratingen, Germany) and slowly advanced toward the hippocampus. The LFP signal was monitored via an audio amplifier (Grass Technologies), and the CA1-PC layer, typically located 1.1–1.3 mm below the brain surface, was identified by the presence of theta-modulated spikes and increased ripple amplitude. The extracellular electrode to be used for the simultaneous LFP recordings was then mounted on a second micromanipulator (Narishige, Amityville, NY) with a 40°–45° angle relative to bregma. This electrode was advanced through the second, more posterior craniotomy until the CA1-PC layer was identified using the same criteria. Two LFP signals were recorded simultaneously to measure the phase shift between the LFP electrode position and the site of whole-cell patch recording. Subsequently, the vertically oriented LFP electrode was replaced with whole-cell patch electrodes (8–12

MΩ) filled with intracellular solution containing (in mM): 134 K-gluconate, 6 KCl, 10 HEPES, 4 NaCl, 0.3 Tris-GTP, 4 MgATP, and 14 Tris-phosphocreatine. Biocytin (0.2%) was added to the intracellular solution. Whole-cell electrodes were vertically advanced through the cortex with 8–9 psi of pressure. Upon entry into the hippocampus (100–200 μm above the depth determined by the LFP measurement), the pressure was reduced to 0.15–0.30 psi. Cells were identified based on reproducible increases in electrode resistances, and then the whole-cell configuration was achieved.

Forty pyramidal neurons were classified as place cells based on their firing characteristics: firing rate in ten consecutive spatial bins (20 cm) exceeded 20% of the peak firing rate, and the mean in-field firing rate was more than three times the mean out-of-field firing rate. Of these, twenty-two were experimentally induced via a BTSP induction protocol, consisting of somatic current injections (300 ms, 800 pA) applied during 6 consecutive laps at the same spatial location, as previously described.[70] For MSOP and dextran experiments, the LFP electrode was filled with a solution containing MSOP (100 μM) or Texas Red dextran 10 KDa (1 mM; Cat# D1828, ThermoFisher Scientific, Waltham, MA). In control experiments, the LFP electrode was only filled with 0.9% saline vehicle solution.

Histology

In some experiments, at the end of the recording session, we replaced the LFP electrode with a new electrode filled with Sulforhodamine 101 (SR-101, 1 mM). This SR-101-filled electrode had a tip resistance of 1.5–3.5 MΩ and was positioned in the same location as the original LFP electrode. We then applied a constant pressure of 0.5 psi for 10 min, to estimate the diffusion distance of drugs pressure applied through the pipette from the SR-101 labeling of astrocytes. Mice were transcardially perfused within 5 min from the end of the electrophysiology experiments, using PBS (20 mL) followed by 4% PFA in PBS (20 mL). Extracted brains remained overnight in 4% PFA and were then rinsed twice and stored in PBS. Then, we prepared 100 μm-thick sagittal sections of PFA-fixed brains using a vibrating blade microtome (VT1000S; Leica Microsystems, Buffalo Grove, IL). The slices were incubated with streptavidin AF488 (1:750) and Triton X-100 0.2% overnight at 4°C, washed 3 times with PBS for 15 min, and mounted on glass slides using Fluoromount G DAPI mounting medium (Cat# 00-4959-52, ThermoFisher Scientific, Waltham, MA). All histological images were acquired on a Nikon Ti2E inverted confocal microscope equipped with 405/488/561/640 nm laser lines and Nikon Elements image acquisition software version 6.10.01.

Antibodies

Information about primary antibodies used for EM is reported below.

Target	Host organism	Source	Primary antibody	Reference	Dilution
mGluR4a	Rabbit	F. Ferraguti	RRID: AB_23147894	Corti et al.[12]	1:300
mGluR7a	Rabbit	Millipore Sigma	RRID: AB_310459	Quraishi et al.[106]; Tomioka et al.[107]	1:70
mGluR8a	Guinea pig	F. Ferraguti	RRID: AB_2314798	Kinoshita et al.[108]	1:100
tdTomato	Goat	OriGene	RRID:AB_2722750	Beattie et al.[109]	1:1,000

The mGluR4a antibody was raised against a fusion protein containing the C-terminal fragment (AA 834–912) of rat mGluR4a.[12] Immunoreactivity in western blots and in fixed brain sections from mGluR4 knock-out mice was totally abolished.[12] The mGluR7 antibody was raised against a peptide corresponding to the C-terminal fragment (AA 899–912) of human mGluR7a (consistent with the mouse sequence). This antiserum recognizes a 97-kDa band on Western blot (manufacturer's technical information) and appears to be specific since the immunostaining pattern is abolished in knock-out mice.[107] The mGluR8a antibody was raised against a peptide corresponding to the mGluR8a mouse C-terminal mGluR8a (AA 886–908[110]). Immunoreactivity in western blots and in fixed brain sections from mGluR8 knock-out mice was totally abolished.[110]

Information about secondary antibodies used for EM is reported below.

Target	Host organism	Source	Secondary antibody	Reference	Dilution
Rabbit IgG	Donkey	Jackson Immunoresearch	RRID: AB_2340594	–	1:250
Guinea pig IgG	Donkey	Jackson Immunoresearch	RRID: AB_2340452	–	1:250
Goat IgG	Donkey	AURION	RRID:AB_2943420	–	1:40

Tissue collection and pre-embedding immunolabeling for EM analysis

The ultrastructural localization of mGluRIII receptors was analyzed using single immunoperoxidase EM in tissue samples from C57BL/6J (n = 2) aged P40. Double immunoperoxidase EM experiments were performed in tissue collected from $PV^{Cre/+}$:$Ai9^{Tg/Tg}$

($n = 2$) and $SST^{Cre/+}$:$Ai9^{Tg/Tg}$ mice ($n = 2$) aged P33-34. In both cases, mice were anesthetized with an intraperitoneal injection of chloral hydrate (4 mg/g, w/w; Cat# 07-894-1075; Patterson Veterinary, Loveland, CO) and perfused transcardially with a flush of 100 mL ice-cold, oxygenated ACSF (80 mL/min) containing (in mM): NaCl 119, KCl 2.5, $CaCl_2$ 0.5, $MgSO_4 \cdot H_2O$ 1.3, $MgCl_2$ 4, $NaHCO_3$ 26.2, NaH_2PO_4 1, glucose 22, pH 7.4 followed by 100 mL PFA4% in 0.1 M phosphate buffer (PB; pH 7.4; 80 mL/min). Brains were removed, post-fixed in the same fixative for 48 h at 4°C. They were washed and transferred to PBS added with an antiproteolytic cocktail (MG132 50 μM, pepstatin 1 μg/mL, leupeptin 20 μM, aprotinin 0.05 U/ml, and phenylmethylilphonyl fluoride 3.6 μM), and stored at 4°C for up to two weeks. Serial parasagittal sections (50 μm thick) were prepared using a vibrating blade microtome (PELCO easi-Slicer, Ted Pella, Redding, CA) and collected in PB until processing.[111]

For single immunoperoxidase pre-embedding studies, hippocampal sections were treated with H_2O_2 (1% in PB; 30 min) to remove endogenous peroxidase activity, rinsed in PB and pre-incubated in 10% Normal Donkey Serum (NDS, 1 h). Sections were then incubated overnight at room temperature (RT) in a solution containing the primary antibody mixture. The following day, sections were rinsed 3 times in PB and incubated first in 10% NDS (15 min) and then in a solution containing the secondary biotinylated antibodies (1.5 h at RT). Sections were subsequently rinsed in PB, incubated in avidin-biotin peroxidase complex (Vectastain Elite ABC-HRP kit, Cat# PK6100, Vector Laboratories, Newark, CA), washed several times in PB, and incubated in 3,3′diaminobenzidine tetrahydrochloride (DAB; 0.05% in 0.05 M Tris buffer, pH 7.6 with 0.03% H_2O_2). Method specificity was verified by substituting the primary antibodies with PB. After completion of the immunoperoxidase procedure, the sections were post-fixed in 1% osmium tetroxide in PB for 45 min and contrasted with 1% uranyl acetate in maleate buffer (pH 6.0; 1 h).[111] The sections were then dehydrated in ethanol and propylene oxide, embedded in Epon/Spurr resin, flattened between Aclar sheets (Cat# 50426-25, Electron Microscopy Sciences, Hatfield, PA) and polymerized at 60°C for (48 h). Section chips including the pyramidal layer and *stratum radiatum* of hippocampal area CA1 were selected by light-microscopic inspection, glued to blank epoxy, and sectioned with an ultramicrotome (MTX, RMC Boeckeler, Tucson, AZ). The most superficial ultrathin sections (∼60 nm) were collected and mounted on copper grids, stained with Sato's lead, and examined with a Philips CM100 transmission electron microscope coupled to a MegaView G2 TEM camera (Evident, Waltham, MA) controlled by software from Soft Imaging System GmbH, Muenster, Germany. To minimize the effects of procedural variables, material from each animal for each antigen was processed in parallel.

For double immunoperoxidase-immunogold labeling studies, following the completion of the immunoperoxidase procedure for mGluR4a, mGluR7a, or mGluR8a, sections were exposed to the pre-embedding immunogold silver enhancement procedure for the identification of of PV/SST-INs via detection of tdTomato in tissue collected from $PV^{Cre/+}$:$Ai9^{Tg/Tg}$ and $SST^{Cre/+}$:$Ai9^{Tg/Tg}$ mice.[112] Briefly, according to Yi et al.[113] and the manufacturer instructions (AURION, Wageningen, the Netherlands) after several rinses in PBS, sections were incubated with a tdTomato goat primary antibody (Cat# AB8181; SICGEN, Cantanhede, Portugal) dissolved in incubation buffer (PBS with 0.2% BSA-c, Cat# 900.022; AURION, Wageningen, the Netherlands) overnight at RT, washed in incubation buffer and then in colloidal gold ultrasmall conjugated anti-goat secondary antibody dissolved in incubation buffer (Cat# 800.333; AURION, Wageningen, the Netherlands) for 4 h at RT and overnight at 4°C. After several rinses in incubation buffer and PBS, the sections were immersed in 2.5% glutaraldehyde in PBS for 1 h, rinsed several times in PBS and in Enhancement Conditioning Solution (ECS Cat# 500.055; AURION, Wageningen, the Netherlands), and then incubated with a silver enhancement reagent (R-Gent SE-EM Cat# 500.044; AURION, Wageningen, the Netherlands) for 60 min under dark conditions. After silver enhancement, the sections were osmicated in 0.5% osmium tetroxide in distillated water for 15 min, then rinsed in distilled water, PBS and last in maleate buffer. The sections were then contrasted with 1% uranyl acetate in maleate buffer (pH 6.0; 1 h) and embedded in Epon/Spurr resin. Section chips including the pyramidal layer and *stratum radiatum* of hippocampal area CA1 were selected by light-microscopic inspection, glued to blank epoxy, and sectioned with an ultramicrotome. The most superficial ultrathin sections (∼60 nm) were collected and mounted on copper grids, stained with Sato's lead, and examined with a Philips CM100 transmission electron microscope.

NEURON model of CA1-PCs

We built a compartmental model of CA1-PCs using the 3D morphology of a biocytin-filled CA1-PC generated previously by our lab (https://www.neuromorpho.org) (Figure S9A). All files pertaining to the NEURON simulations were uploaded to the ModelDB database (https://modeldb.science/2031084, ModelDB acc.n. 2031084). The NEURON model was created to reproduce the results of the voltage-clamp experiments described in Figures 5B–5I and was run on Microsoft Visual Studio Code as an IDE. In this model, the CA1-PC was voltage-clamped at 0 mV, and a leak potassium conductance (g_{pas}) was used to reproduce space clamp errors associated with somatic voltage-clamp recordings[66,114] (Figures S9B–S9D). We used NRN-EZ (v1.1.6)[115] to randomly distribute 100 I-inputs along the soma and apical dendrites and set $g_{pas} = 10^{-5}\left(e^{d/100}\right)$ (S/cm^2), where d = distance between the soma and each compartment expressed in μm (Figures S9B–S9D).

Once the relationship between g_{pas} and d was set, we performed separate simulations to constrain the synaptic weight of each inhibitory input. This was done empirically, working under the assumption that in many neocortical neurons voltage escape prevents recording the activity of synaptic inputs located >200 μm from the soma.[66,116,117] This synaptic weight was set to 485 pS for both PV- and SST-inputs, to generate somatic mIPSCs with a mean amplitude of 12.8 pA, similar to the one recorded experimentally (12.7 ± 1.0 pA, $n = 10$; Figures 3A and 3B; Figures S9E and S9F). The local rise and exponential decay time of the I-inputs in the model were set to 1.5 and 20.0 ms, respectively, to ensure that the mIPSC kinetics at the soma matched those recorded experimentally (mIPSC rise model = 3.4 ms, t_{50} model = 17.8 ms; mIPSC rise exp = 3.6 ± 0.1 ms, t_{50} exp = 17.8 ± 0.9 ms $n = 10$; Figures 3A and 3B). We

constrained the release probability of PV- and SST-INs synapsing onto CA1-PCs based on previous work indicating that $Pr_{PV} = 0.8$ at $\left[Ca^{2+}\right]_o = 2$ mM[68] (Figure S9G). Given that there is a 4th power relationship between Pr and $\left[Ca^{2+}\right]_o$ [19,67], we estimated $Pr_{PV} = 0.1$ at $\left[Ca^{2+}\right]_o = 1.2$ mM, which we used in our recording conditions (Figure S9G). Based on our optogenetics experiments, the number of active PV release sites required to evoke an oIPSC comparable to the oIPSC evoked experimentally is 4. Therefore, we estimated a total of 4/0.1 = 40 PV release sites targeted CA1-PC in our model. EM data indicate that there are 8.3 times more SST-than PV-inputs onto CA1-PCs.[69] Therefore, the total number of SST release sites was estimated as 40·8.3 = 332. The number of active SST sites required to generate an oIPSC with the same amplitude as the oIPSC recorded experimentally was 18, leading to Pr_{SST} = 18/332 = 0.05 (Figure S9G). Each simulation was repeated 100 times, each time randomizing the location of the active inputs. Therefore, the results represent the average of 100 simulations.

EM analysis

Immuno-positive profiles were studied from ultrathin sections at the surface of the embedded blocks. Quantitative data on profiles derived from the analysis of hippocampal neuropil (10–15 ultrathin sections/mouse; 2 mice for each antigen). Fields of view with mGluR4a, mGluR7a, and mGluR8a positive profiles were randomly selected, and captured at 19,000–34,000× magnification. Acquisition of microscopical fields and analysis were performed under blinded conditions. For the analysis of the distribution of mGluRIII positive profiles, subcellular compartments (i.e., dendrites, axons, axon terminals, and astrocytic processes) were identified according to well-established criteria.[118] In line with previous quantitative EM of synapses,[119] in a synapse the pre-synaptic terminal was characterized by vesicles adjacent to the pre-synaptic density, the synaptic cleft displayed electrodense material, the pre- and post-synaptic membranes defining the pre- and post-synaptic specializations were characterized by electron densities, and finally the prominent and/or thin post-synaptic density in addition to clear and round or pleiomorphic vesicles permitted to distinguish asymmetric and symmetric synapses.[111,119] According to different post-synaptic targets of interneurons, immuno-positive axon terminals forming symmetric synaptic contacts were sampled at axo-somatic, proximal, distal, or spinous axo-dendritic synapses (dendrites were considered distal if their diameter was $\leq$1 μm, proximal if it was >1 μm.[120–124] Astrocytic processes were identified by their typical irregular outlines, the paucity of cytoplasmic components (except for ribosomes, glycogen granules, and some bundles of fibrils.[118] Pre-embedded double labeled material, EM inspection of ultrathin sections (10–12 per mouse/antigen) allowed identifying axon terminals of PV- and SST-INs based on the presence of silver amplified signal within terminals synapsing with post-synaptic domains and to recognize electron-dense immunoreacted products relative to mGluRIII isoforms in the close vicinity of the active zone.

In vitro electrophysiology analysis

Electrophysiological recordings were analyzed within the Igor Pro environment using custom made software (A. S.). EM data were analyzed within the GraphPad Prism environment.

In vivo electrophysiology and behavior analysis

We analyzed the *in vivo* electrophysiology and behavioral data using custom code written in MATLAB 2023b (Mathworks, Natick, MA). The analysis was performed on periods of time when the mouse was running at a speed of >4 cm/s. Action potentials were detected using the first derivative of the raw V_m, as the time points when its depolarization rate crossed a threshold of 40 mV/ms. To analyze the slow V_m, we removed action potentials from the raw traces, replaced them using a linear interpolation of the raw V_m, down-sampled the resulting V_m to 200 Hz, and then low-pass filtered them at 2 Hz using a finite impulse response (FIR) filter with a 2 s Hamming window. To ensure that V_m and slow V_m had the same number of data points, we resampled the slow V_m at 20 kHz. The baseline value of the slow V_m was defined as the mode of the slow V_m calculated over the entire recording. This value was subtracted from the slow V_m to calculate the absolute amplitude of the V_m ramp depolarization for each bin. To calculate the intracellular theta amplitude, we applied a Hilbert transform to the subthreshold V_m (i.e., the AP-removed but unfiltered V_m), after it was down-sampled to 200 Hz, band-pass filtered at 4–7 Hz (2 s Hamming window) and re-sampled at 20 kHz. For each cell, the action potential frequency, the slow V_m, baseline V_m-corrected V_m, and intracellular theta amplitude were calculated over 2 cm bins and averaged across 20–40 laps. Among all recorded neurons, place cells were identified using spatially binned mean action potential firing rate maps and defined as neurons exhibiting at least a 3-fold increase in firing rate across at least three contiguous bins (6 cm total) compared to out-of-field locations. Only neurons meeting this criterion were included in subsequent analyses. To compare the effects of MSOP and dextran application across the entire length of the track (Figures 6C, 6F,6I, and 6L; Figures S13B, S13E, S13H, and S13K), mean spatial activity maps were peak-aligned and averaged across cells. Effects of MSOP and dextran on spatial selectivity were quantified as previously described.[101] Briefly, for slow V_m, baseline-corrected V_m, and action potential firing rate, we computed the average activity across 10 bins (i.e., 20 cm) centered around the maximum (peak in-field) or minimum (lowest out-of-field) values. This approach was chosen to assess the effect of mGluRIII inhibition at spatial locations with different excitation/inhibition ratios. For data shown in

Figure S11A, the subthreshold V_m ramp width was calculated as the distance over which the subthreshold V_m exceeded 20% of the maximum values. The spatial information per spike (I; Figure S11C) was calculated using the formula developed by Skaggs et al., 1992[125]:

$$I = \sum_{i=1}^{N} p_i \frac{\lambda_i}{\lambda} \log_2\left(\frac{\lambda_i}{\lambda}\right),$$

where i = number of non-overlapping spatial bins; p_i = occupancy probability of bin i; λ_i = mean firing rate for bin i (bin size: 2 cm); λ = overall mean firing rate of the place cell across the entire environment. I is expressed in bits per spike. The place field sparsity (S; Figure S11D), which measures the fraction of the environment over which the place cell is active, was calculated as the adaptation of the formula invented by Treves & Roll (1991).[126] The formula is:

$$S = \frac{\left(\sum p_i \lambda_i\right)^2}{\sum p_i \lambda_i^2}$$

Place field size Figure S11F) was measured as the distance over which the firing rate exceeded 20% of its peak value.

QUANTIFICATION AND STATISTICAL ANALYSIS

Data are presented as mean ± SEM unless otherwise stated. Normality was tested using SPSS or GraphPad Prism 8.2.1. Statistical significance was determined by Student's paired or unpaired *t* test, ANOVA, Generalized Estimated Equations (GEE; Figures 2S–2V; Figures 6C, 6F, 6I, and 6L; Figures S10C, S10E, S10I, and S10K; Figures S11B and S11E; Figures S13B, S13E, S13H, and S13K) or Fisher exact test (EM data in Tables 1 and 2), as appropriate (IgorPro 6.37, SPSS, GraphPad Prism 8.2.1). Differences were considered significant at $p < 0.05$ ($^*p < 0.05$; $^{**}p < 0.01$; $^{***}p < 0.001$).